TMT4920 Materials Technology, Master's Thesis

Summer 2020

Return-mapping algorithm for rate-independent crystal yield surface

Hassan Moradi Asadkandi

Supervisor: Professor Bjørn Holmedal

Co-Supervisor: Dr. Tomás Mánik

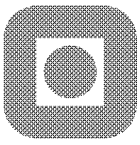

Department of Materials Science and Engineering

Norwegian University of Science and Technology,

NTNU

Abstract:

The main target of this work was to develop a stable and fast numerical algorithm for crystal plasticity with arbitrary slip systems and crystal elasticity. By the use of a regularized yield surface, the methods from the continuum plasticity are applicable, where the plasticity models are solved with integration over time as they are presented in the form of rate equations. For this purpose, the integration of the local constitutive equations is carried out by an iterative process which includes solving for elastic and plastic parts of the total strain increment, and eventually, updating the stress and internal state variables. This MSc work studies the implementation of a fully implicit Newton-Raphson method, modified with a line search algorithm for solving the return mapping problem. Firstly the isotropic Hosford yield surface for continuum plasticity is considered for validating the algorithms, then a crystal plasticity yield surface with a high exponent is approached. The line search algorithm is proved to be very robust and efficient. Improving the first guess makes it even more efficient. The statistical analysis regarding the convergence behavior of the models is presented and the potential for further improvement is discussed.

Table of Contents

1 Introduction

Numerical simulation of the metal forming processes is now one of the main methods to investigate the behavior of parts and products in sophisticated manufacturing conditions. The simulation programs used in industry are based on the material models of the plastic deformation of metals. The efficiency and accuracy of such finite element codes that are used for solid mechanics analysis, is influenced by the constitutive models they use. In consequence, a vast number of plasticity models are proposed in the literature and used in finite element calculations.

Industrial materials that can undergo a plastic deformation often have an elastic range with a purely elastic response. This range is defined by a closed domain in stress or strain space and its boundary is called the yield surface. This boundary is defined by a yield criterion which is the main feature of most plasticity models.

Mechanical properties of metals are considerably influenced by their complex anisotropic microstructure. In a single crystal, plastic flow is anisotropic and therefore cannot be modeled using a simple constitutive equation that doesn't consider the slip activity in the crystal. [1] Crystal plasticity models take into account the microstructure, grain orientations, and their plastic properties to derive macroscopic properties like the yield surface, through multiscale modeling. In other words, the prominent aspect of crystal plasticity theory is the explicit modeling of slip systems within the crystal lattice to establish a model that explains the plastic slip.

Such models, when implemented in numerical simulations, are capable of a more accurate estimation of the material response. furthermore, by modeling the rotations of individual grains in polycrystalline materials, they predict the evolution of texture and therefore, account for the anisotropic effects arisen from texture and grain shapes.

The objective of this work is to implement a return mapping algorithm for obtaining rate-independent crystal yield surface and to study the achievable improvements by using modifications proven to be effective for other models.

1.1 Notational Convention

A coordinate-free approach is used in this work to present the structure of models and other governing equations in a convenient manner. To denote vectors, a vector symbol above the letter is used whereas bold-face letters refer to second-order tensors. For the fourth-order tensors, an outline capital letter is used. Scalar parameters are presented with italic normal letters. This approach is summarized in table 1:

	Scalar	Vector	Second-order tensor	Fourth-order tensor
Latin	a	$\vec{a}$	$\boldsymbol{A}$	$\mathbb{A}$
Greek	α, λ	$\vec{\sigma}$	$\boldsymbol{\sigma}$	

Table 1- Notational convention employed in this work.

The cartesian components of vectors and tensors are referred to as: a_i, $A_{ij,}$ and A_{ijkl}.

Moreover, to simplify the operations and increase the running speed of the solution, and since the stress is a symmetric tensor, Mandel-Notation is used. By reducing the order of tensor, the original [3x3] tensor is reduced to a [1x6] vectors, as described below:

In matrix notation, the stress tensor is represented as:

$$\boldsymbol{\sigma} = \begin{bmatrix} \sigma_{11} & \sigma_{12} & \sigma_{13} \\ \sigma_{21} & \sigma_{22} & \sigma_{23} \\ \sigma_{31} & \sigma_{32} & \sigma_{33} \end{bmatrix}$$

In Voigt notation, it is simplified to a [1x6] vector where only six components are used: the three on the diagonal, and the others being off-diagonal components:

$$\vec{\sigma} = \begin{bmatrix} \sigma_{11} & \sigma_{22} & \sigma_{33} & \sigma_{23} & \sigma_{13} & \sigma_{12} \end{bmatrix}$$

Mandel notation uses the same components from the original tensor but all the off-diagonal components will be multiplied by $\sqrt{2}$.

$$\vec{\sigma} = \begin{bmatrix} \sigma_{11} & \sigma_{22} & \sigma_{33} & \sqrt{2}\,\sigma_{23} & \sqrt{2}\,\sigma_{13} & \sqrt{2}\,\sigma_{12} \end{bmatrix}$$

The main advantage of using Mandel notation is that it allows using the same conventional operations used with vectors. for example, when calculating the $\boldsymbol{\sigma}:\boldsymbol{\sigma}$ for the original [3x3] tensor, which is equal to the square root of the sum of the squares of the tensor components, using Voigt notation will not give the same result as the original second-order tensor. Mandel notation, however, will count for the double appearance of the off-diagonal components by using the $\sqrt{2}$ coefficient.

The other advantage of using the Mandel form of tensors is avoiding fourth-order tensor operations. For instance, the fourth-order [3x3x3x3] stiffness and compliance matrices which were reduced to [6x6] matrices by using the minor symmetries (resulted from the symmetry of the stress and strain tensors) can be represented in Mandel notation. Such symmetric tensor of rank four with only 36 distinct components can be expressed in Mandel Notation as:

$$\boldsymbol{C} = \begin{pmatrix} C_{1111} & C_{1122} & C_{1133} & \sqrt{2}C_{1123} & \sqrt{2}C_{1113} & \sqrt{2}C_{1112} \\ C_{2211} & C_{2222} & C_{2233} & \sqrt{2}C_{2223} & \sqrt{2}C_{2213} & \sqrt{2}C_{2212} \\ C_{3311} & C_{3322} & C_{3333} & \sqrt{2}C_{3323} & \sqrt{2}C_{3313} & \sqrt{2}C_{3312} \\ \sqrt{2}C_{2311} & \sqrt{2}C_{2322} & \sqrt{2}C_{2333} & 2C_{2323} & 2C_{2313} & 2C_{2312} \\ \sqrt{2}C_{1311} & \sqrt{2}C_{1322} & \sqrt{2}C_{1333} & 2C_{1323} & 2C_{1313} & 2C_{1312} \\ \sqrt{2}C_{1211} & \sqrt{2}C_{1222} & \sqrt{2}C_{1233} & 2C_{1223} & 2C_{1213} & 2C_{1212} \end{pmatrix}$$

In the case of stiffness and compliance matrices, the most general anisotropic linear elastic material will have 21 material constants and the matrix above will be symmetric.[1]

Using Mandel notation will replace the ":" operator (double dot production) between two tensors with matrix multiplication as described. in indicial notation:

$$\text{if } \mathbf{A} \text{ and } \mathbf{B}, \text{both rank two tensors } \rightarrow \quad \boldsymbol{A}:\boldsymbol{B} = A_{ij}B_{ij}$$

$$\text{if } \mathbb{A} \text{ a rank four tensor and } \mathbf{B} \text{ a rank two tensor } \rightarrow \quad \mathbb{A}:\boldsymbol{B} = A_{ijkl}B_{kl}\boldsymbol{e}_i \otimes \boldsymbol{e}_j$$

But when written in Mandel notation, second-order tensors will be converted to vectors and fourth-order tensors will be reduced to second-order tensors, considerably decreasing the calculation load. This operation will affect double dot production as followed:

$$\boldsymbol{A}:\boldsymbol{B} = \vec{a} \cdot \vec{b}$$

$$\mathbb{A}:\boldsymbol{B} = \boldsymbol{A} \cdot \vec{b}$$

To have the formulations similar to the way they are implemented in the code, they are presented in Mandel notation as much as possible. If stress and strain tensors are written as vectors, and elastic moduli in a second-order tensor mode, the Mandel notation is employed.

2 Theoretical background

The topics studied in this work, mainly include yield functions, crystal plasticity model, and general closest point projection algorithm. Each of them will be introduced and reviewed briefly in the following.

2.1 Yield function

A yield surface is defined as a surface in stress space such that it bounds stress states which can be reached without initiating plastic strains. Mathematically, this surface can be represented by a yield function. Over the past two centuries, several yield criteria have been proposed. Although the two criteria commonly attributed to von Mises and Tresca are the most representative of initial yielding in metallic isotropic materials. [2]

2.1.1 Von misses yield function

This criterion is based on the determination of the energy associated with shape change (distortion energy) in a material. According to von Mises's theory, a ductile solid will yield when the maximum value of the distortion energy per unit volume reaches a critical value for that material. This criterion should hold for the uniaxial stress state and therefore, the critical value of the distortional energy can be obtained from the uniaxial test. [3]

Mathematically, the yield function for the von Mises criterion suggests that the yielding of material begins when the von Mises stress reaches the yield stress σ_y:

$$f(\boldsymbol{\sigma}) = \sigma_v - \sigma_y = 0 \tag{1.1}$$

Where σ_v can be expressed in terms of the deviatoric stress of $\boldsymbol{\sigma}'$ and second deviatoric stress invariant, J_2, as follows:

$$\sigma_v = \sqrt{3J_2} = \sqrt{\frac{3}{2}\boldsymbol{\sigma}' : \boldsymbol{\sigma}'} \quad , \; \boldsymbol{\sigma}' = \boldsymbol{\sigma} - \frac{1}{3}\big(\mathrm{tr}(\boldsymbol{\sigma})\big)\boldsymbol{I} \tag{1.2}$$

This yield criterion can be stated in principal stress components as [2]:

$$(\sigma_1 - \sigma_2)^2 + (\sigma_2 - \sigma_3)^2 + (\sigma_3 - \sigma_1)^2 = 2{\sigma_y}^2 \quad (1.3)$$

And as a function of stress tensor components:

$$(\sigma_{11} - \sigma_{22})^2 + (\sigma_{22} - \sigma_{33})^2 + (\sigma_{33} - \sigma_{11})^2 + 6({\sigma_{23}}^2 + {\sigma_{31}}^2 + {\sigma_{12}}^2) = 2{\sigma_y}^2 \quad (1.4)$$

This yield criterion can be defined as a circular cylinder which forms a circle in an intersection with the deviatoric plane with the radius of $\sqrt{\frac{2}{3}}\sigma_y$, as shown in figure 1.

2.1.2 Tresca yield function

The second yield criterion presented in this section has a very direct physical interpretation. According to the Tresca yield criterion, yielding in a material starts when the maximum shear stress reaches the Tresca yield shear stress which is determined by uniaxial stress. This criterion is also known as the maximum shear stress criterion and represents the yield criterion for the Tresca material model. [3] Mathematically it can be represented as:

$$\tau_{max} = \frac{1}{2}(\sigma_{max} - \sigma_{min}) \quad (1.5)$$

Where σ_{max} and σ_{min} are the maximum and minimum principal stresses in the material. In the case of the uniaxial stress, $\sigma_1 = \sigma_y$ and $\sigma_2 = \sigma_3 = 0$, therefore the maximum shear stress of this criterion will be:

$$\tau_{max} = \frac{\sigma_y}{2} \quad (1.6)$$

In the principal stress space, as shown in figure 1, this criterion is represented by a regular hexagonal cylindrical yield surface with a regular hexagonal yield curve.

Tresca yield criterion is arguably more conservative failure theory than distortion energy theory or von Mises criterion since it is contained within the latter. Certain stress states that happen to exist between these two yield surfaces are considered to fail according to the Tresca yield criterion whereas according to the von Mises criterion they should still be in the elastic domain.

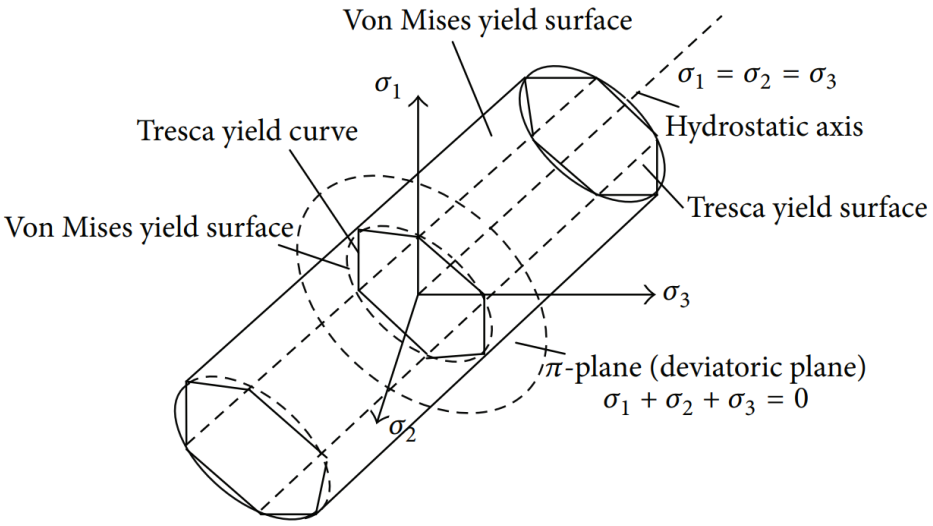

Figure 1- The mathematical representation of the von Mises and Tresca yield surfaces, in three-dimensional stress space. [4]

2.1.3 Hosford yield function

The Hosford yield criterion is a generalization of the von Mises and Tresca yield surfaces and often lies between these two yield surfaces. The value of exponent "*a*" in the expression of effective stress defines the shape of the final yield surface. If "*a*" is chosen to be 2 or 4, the yield surface will be a von Mises yield surface. however, if $a = 1$ or in the limit as $a \rightarrow \infty$, the yield surface is a Tresca yield surface. for $1<a<2$ and $4<a<\infty$ the yield surface lies between the two yield surfaces.[5]

Depending on the choice of the exponent "*a*", the Hosford model is the description of the yield surface for the material. The plastic flow direction can be obtained using the associated flow rule.

The yield function which defines the yield surface is given by:

$$f(\boldsymbol{\sigma}) = \varphi(\boldsymbol{\sigma}) - \sigma_y \tag{1.7}$$

Where φ is the effective stress of the Hosford Model which is given by:

$$\varphi(\boldsymbol{\sigma}) = \left\{\frac{1}{2}\left[|\sigma_1 - \sigma_2|^a + |\sigma_2 - \sigma_3|^a + |\sigma_3 - \sigma_1|^a\right]\right\}^{1/a} \tag{1.8}$$

The exponent "a" is a material model parameter and σ_i are the principal stress values.

σ_y in yield function expression depends on the hardening law, which can be defined separately. For the case of perfect plasticity which is considered to be the case in this work, it is equal to the yield strength. If the hardening of material is also to be considered, then the equivalent plastic strain should also be given to the yield function in any iteration of the solution.

To find the principal stress values, σ_i, in the effective stress equation, three eigenvalues and eigenvectors of the given stress tensor is found using the numpy.linalg.eig function. For the stress tensor $\boldsymbol{\sigma}$, these will be the principal stresses and their directions. This library uses LAPACK ("Linear Algebra Package") routine for solving the eigenvalue problems. LAPACK is a standard software library for numerical linear algebra. [6]

To avoid numerical overflow problem when calculating effective stress, the principal stresses in this expression are scaled with von Mises stress.

By using von Mises stress for scaling, effective stress can be obtained by the following expression:

$$\varphi(\boldsymbol{\sigma}) = \sigma_v \left\{\frac{1}{2}\left[|\bar{\sigma}_1 - \bar{\sigma}_2|^a + |\bar{\sigma}_2 - \bar{\sigma}_3|^a + |\bar{\sigma}_3 - \bar{\sigma}_1|^a\right]\right\}^{1/a} \quad , \quad \bar{\sigma}_i = {}^{\sigma_i}/_{\sigma_v} \tag{1.9}$$

For integrating the model and solving the return mapping with an incremental solution, first and second derivatives (normal to the yield surface and Hessian, respectively) of the effective stress are needed. The following expressions are used for this purpose, as derived and presented by Scherzinger (2016) [7].

The first derivative can be expressed in terms of the principal stress directions, $\hat{\mathbf{e}}_i$ (eigenvectors of the given stress tensor):

$$\frac{\partial \varphi}{\partial \boldsymbol{\sigma}} = \sum_{i=1}^{3} \frac{\partial \varphi}{\partial \sigma_i} \hat{\boldsymbol{e}}_i \otimes \hat{\boldsymbol{e}}_i \tag{1.10}$$

The partial derivatives are given by equation 1.11 and to avoid numerical overflow and to improve the accuracy, another scaling is applied, using the value of the effective stress. The other partials can be obtained using the same pattern:

$$\frac{\partial \varphi}{\partial \sigma_1} = \frac{1}{2}[(\hat{\sigma}_1 - \hat{\sigma}_2)|\hat{\sigma}_1 - \hat{\sigma}_2|^{a-2} - (\hat{\sigma}_3 - \hat{\sigma}_1)|\hat{\sigma}_3 - \hat{\sigma}_1|^{a-2}], \quad \hat{\sigma}_i = {}^{\sigma_i}/_{\varphi} \tag{1.11}$$

The second derivative of the effective stress with respect to the stress is also presented based on eigenvectors:

$$\frac{\partial^2 \varphi}{\partial \boldsymbol{\sigma} \partial \boldsymbol{\sigma}} = H_{ijkl}\, \hat{\mathbf{e}}_i \otimes \hat{\mathbf{e}}_j \otimes \hat{\mathbf{e}}_k \otimes \hat{\mathbf{e}}_l \tag{1.12}$$

Where the non-zero H_{ijkl} components can be obtained using the following patterns and permuting the indices:

$$H_{1111} = \frac{\partial^2 \varphi}{\partial \sigma_1 \partial \sigma_1} \quad , \quad H_{1122} = \frac{\partial^2 \varphi}{\partial \sigma_1 \partial \sigma_2} \tag{1.13}$$

$$H_{1212} = \frac{1}{2} \frac{\partial \varphi / \partial \sigma_1 - \partial \varphi / \partial \sigma_2}{(\sigma_1 - \sigma_2)} \tag{1.14}$$

When $(\sigma_1 - \sigma_2) = 0$ in equation 1.14, it can be obtained by equation 1.15 which is derived using the limit.

$$H_{1212} = \frac{1}{2}\left(\frac{\partial^2 \varphi}{\partial \sigma_1 \partial \sigma_1} - \frac{\partial^2 \varphi}{\partial \sigma_1 \partial \sigma_2}\right) \tag{1.15}$$

And finally, the second derivatives of the effective stress are to be obtained with equations 1.16 and 1.17, using the scaled principal stresses:

$$\frac{\partial^2 \varphi}{\partial \sigma_1 \partial \sigma_1} = \frac{a-1}{\varphi}\left\{\frac{1}{2}[|\hat{\sigma}_1 - \hat{\sigma}_2|^{a-2} + |\hat{\sigma}_3 - \hat{\sigma}_1|^{a-2}] - \frac{\partial \varphi}{\partial \sigma_1}\frac{\partial \varphi}{\partial \sigma_1}\right\} \tag{1.16}$$

$$\frac{\partial^2\varphi}{\partial\sigma_1\partial\sigma_2} = \frac{a-1}{\varphi}\left\{-\frac{1}{2}|\hat{\sigma}_1 - \hat{\sigma}_2|^{a-2} - \frac{\partial\varphi}{\partial\sigma_1}\frac{\partial\varphi}{\partial\sigma_2}\right\} \tag{1.17}$$

with the other non-zero derivatives following the same pattern.

2.2 Crystal Plasticity

The concept of crystal plasticity relies on the precise knowledge of the kinematics of plastic slip with respect to the crystallographic slip systems. It tries to explain the plastic deformation according to the driving force for the activation of plastic slip, namely the corresponding resolved shear stress, which will be discussed in the following.

Unlike the elastic response of crystalline materials that may be approximated by an isotropic description, the plastic deformation of a single crystal has an anisotropic nature which can be explained by the presence of a finite number of distinct slip systems that are defined by its crystalline structure. [8]

2.2.1 Schmid's law

The extent of the slip in a single crystal is determined by the magnitude of the shear stress resulted from external loads. Depending on the orientation of the grain with respect to the applied load, the produced shear stress can differ between zero to a maximum magnitude, determined by the angles formed between the applied load, normal of the slip plane, and the slip direction, as shown in figure 2. [9] This statement is now commonly referred to as Schmid's law.

In mathematical terms, Schmid's law can be presented as follows:

$$\tau = \sigma\, cos\varphi \cos\lambda$$

Where φ and λ are the angles that slip plane normal and slip direction make with the loading axis, respectively. The factor $cos\varphi \cos\lambda$ in this equation is called the Schmid's factor. [10]

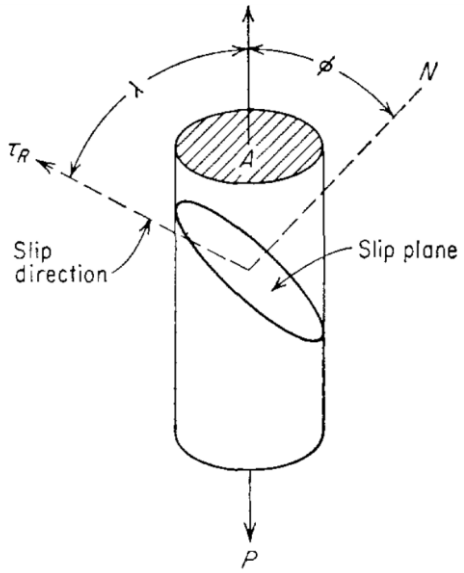

Figure 2- A single crystal specimen subjected to uniaxial tension, highlighting the slip and normal unit vectors of an arbitrary slip system [9]

Assuming that the axial stress is constant, the resolved shear stresses on each slip system will be different, depending on the angles that plane's normal and slip direction make with the axis of loading, and plastic slip occurs in the one for which the resolved shear stress is maximum and has reached a critical value, referred to as the critical resolved shear stress, τ_c. Critical resolved shear stress is a material property and has to be determined experimentally. [10] All the physical conditions of the material that affects dislocation movement in a crystal lattice including temperature, dislocation density, impurities as well as loading condition such as strain rate, can influence the value of the critical resolved shear stress. [11]

For the slip system α, if $\vec{m}^{\alpha}$ is the slip plane normal unity vector, and $\vec{n}^{\alpha}$ the slip direction unity vector, Schmid's equation can be written in terms of these vectors:

$$\boldsymbol{P}^{\alpha} = \frac{1}{2}(\vec{m}^{\alpha} \otimes \vec{n}^{\alpha} + \vec{n}^{\alpha} \otimes \vec{m}^{\alpha}) \tag{1.18}$$

$$\tau = \boldsymbol{\sigma} : \boldsymbol{P}^{\alpha} \tag{1.19}$$

An FCC crystal contains 12 slip systems, considering four octahedral planes with three close-packed directions on each plane. Slip plane normal and slip direction unity vectors for these 12 slip systems are presented in Table 2. [12]

α	$\vec{m}^{\alpha}$	$\vec{n}^{\alpha}$	α	$\vec{m}^{\alpha}$	$\vec{n}^{\alpha}$
1	$1/\sqrt{3}\,(1,1,1)$	$1/\sqrt{2}\,(1,\bar{1},0)$	7	$1/\sqrt{3}\,(1,\bar{1},1)$	$1/\sqrt{2}\,(1,1,0)$
2	$1/\sqrt{3}\,(1,1,1)$	$1/\sqrt{2}\,(0,1,\bar{1})$	8	$1/\sqrt{3}\,(1,\bar{1},1)$	$1/\sqrt{2}\,(0,1,1)$
3	$1/\sqrt{3}\,(1,1,1)$	$1/\sqrt{2}\,(1,0,\bar{1})$	9	$1/\sqrt{3}\,(1,\bar{1},1)$	$1/\sqrt{2}\,(1,0,\bar{1})$
4	$1/\sqrt{3}\,(\bar{1},1,1)$	$1/\sqrt{2}\,(1,1,0)$	10	$1/\sqrt{3}\,(1,1,\bar{1})$	$1/\sqrt{2}\,(1,\bar{1},0)$
5	$1/\sqrt{3}\,(\bar{1},1,1)$	$1/\sqrt{2}\,(0,1,\bar{1})$	11	$1/\sqrt{3}\,(1,1,\bar{1})$	$1/\sqrt{2}\,(0,1,1)$
6	$1/\sqrt{3}\,(\bar{1},1,1)$	$1/\sqrt{2}\,(1,0,1)$	12	$1/\sqrt{3}\,(1,1,\bar{1})$	$1/\sqrt{2}\,(1,0,1)$

Table 2- Slip direction and slip plane normal with respect to an orthonormal basis for the FCC crystal.

2.2.2 Rate independent crystal yield surface

Based on equation 1.19, the strain-rate independent crystal yield surface can mathematically be expressed as the following yield criteria :

$$|\tau| = |\boldsymbol{\sigma} : \boldsymbol{P}^{\alpha}| \leq \tau_c^{\alpha} \tag{1.20}$$

Where τ_c^{α} is the critical resolved shear stress for slip, on slip system α. This equation defines a convex envelope of the linear facets from each slip system.

If slip on a certain slip plane occurs with different critical resolved shear stresses for forward and reverse slip, the yield surface should consider them as two different slip systems, sharing the same plane, yet with opposite slip direction vectors. This study assumes all the critical resolved shear stress values for all slip systems to be the same but the structure of code will be based on 24 slip systems to set a flexible framework for further development.

The inner envelope of the yield surfaces for all the slip systems given by equation 1.20 is expressed as:

$$f(\boldsymbol{\sigma}) = \left(\sum_{\alpha=0}^{N} \left\langle \frac{\boldsymbol{\sigma} : \boldsymbol{P}^{\alpha}}{\tau_c^{\alpha}} \right\rangle^{n} \right)^{\frac{1}{n}} - 1 = 0 \tag{1.21}$$

This equation serves as the yield function of the model and to be able to perform the incremental solution presented in the next section, first and second derivatives with respect to the stress tensor are required. The following expressions presented by Holmedal and Mánik are used for this purpose:

$$\frac{\partial f}{\partial \boldsymbol{\sigma}} = \sum_{\alpha=0}^{N} \left\langle \frac{\boldsymbol{\sigma} : \boldsymbol{P}^{\alpha}}{(f+1)\tau_c^{\alpha}} \right\rangle^{n-1} \frac{1}{\tau_c^{\alpha}} \boldsymbol{P}^{\alpha} \tag{1.22}$$

$$\frac{\partial^2 f}{\partial \boldsymbol{\sigma} \partial \boldsymbol{\sigma}} = \frac{(n-1)}{(f+1)} \left(\sum_{\alpha=0}^{N} \left\langle \frac{\boldsymbol{\sigma} : \boldsymbol{P}^{\alpha}}{(f+1)\tau_c^{\alpha}} \right\rangle^{n-2} \frac{\boldsymbol{P}^{\alpha} \otimes \boldsymbol{P}^{\alpha}}{(\tau_c^{\alpha})^2} - \frac{\partial f}{\partial \boldsymbol{\sigma}} \otimes \frac{\partial f}{\partial \boldsymbol{\sigma}} \right) \tag{1.23}$$

2.3 Return mapping algorithm

The classical plasticity models are solved with integration over time as they are presented in the form of rate equations. such solutions involve the integration of the local constitutive equations by an iterative process. These local integration algorithms should be solved for elastic and plastic parts of the total strain increment, and eventually, update the stress and internal state variables. For non-trivial elastoplastic models, this procedure is done in two main steps. Initially, the strain increment is assumed to be purely elastic. The outcome of such an assumption then should be corrected by subsequent steps that maps the stress onto a suitably updated yield surface. this procedure is referred to as the return mapping algorithm. [13] Figure 3 demonstrates the geometric interpretation of this process in stress space.

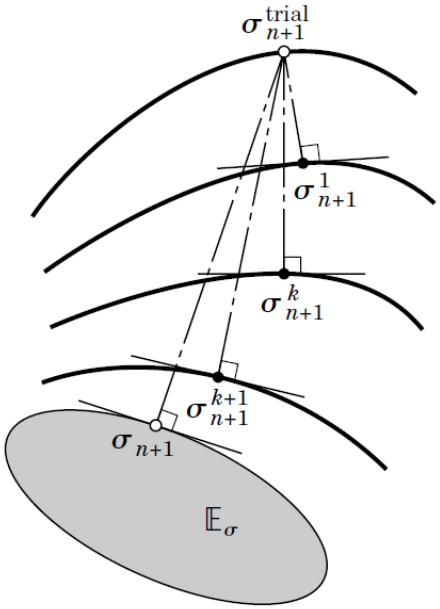

Figure 3- A geometric interpretation of the iteration scheme for the return mapping algorithm. [14]

For the case of isotropic von Mises plasticity models, since the normal to the yield surface is identical to the normal calculated from the trail stress (due to the shape of this specific yield surface in 5-dimensional stress space), the return mapping will be simplified to radial return map that can obtain the final solution in one iteration only. [13]

However, for a single crystal with anisotropic behavior, this will bot be the case since the predictor and corrector flow directions will not be equivalent. In this case, the algorithm should enforce the normality condition by solving for the amount and direction of the plastic flow. [13] This procedure requires a considerable amount of additional computational load that can be an obstacle for implementing it in large scale simulations. For that reason, numerous studies have been conducted to increase the efficiency of these algorithms.

the governing formulations defining the framework of the return mapping algorithm will be presented in the next chapter.

3 Method

3.1 Return Mapping Algorithm

In this section, the overall procedure of the numerical implementation of the Hosford, as well as rate-independent regularized crystal yield surface using a return mapping algorithm, is presented.

3.1.1 Step 1: Trial Stress

Having the initial stress and strain increment, trail stress is calculated, with the assumption that the strain increment is elastic (Elastic Predictor).

$$\boldsymbol{\sigma}_{n+1}^{trial} = \boldsymbol{\sigma}_n + \mathbb{C} : \Delta\boldsymbol{\varepsilon} \tag{3.1}$$

When tensors are provided in Mandel notation:

$$\vec{\sigma}_{n+1}^{trial} = \vec{\sigma}_n + \boldsymbol{C} \cdot \Delta\vec{\varepsilon} \tag{3.2}$$

All the following equations in this chapter assume that the tensors are presented in Mandel notation.

Next is to determine if such trail stress causes plastic deformation. Using the yield function of the Hosford Model (eq x) or the crystal plasticity model (eq x):

$$\text{if } f\left(\vec{\sigma}^{trial}\right) \leq 0 \;\; \rightarrow \;\; \text{the strain increment is elastic and } \vec{\sigma}^{trial} \text{ will be the true } \vec{\sigma}_{n+1}$$

$$\text{if } f\left(\vec{\sigma}^{trial}\right) > 0 \rightarrow \;\; \text{plastic deformation occurs and return mapping will be used to find } \vec{\sigma}_{n+1}$$

To have a uniform distribution of trail stresses and with the goal of comparing with some existing results in the literature, instead of providing initial stress state and the strain increment, trial stresses are given as an input to the model. It's worth mentioning that if the chosen trial stresses include a statistically uniform distribution of stress states with large enough magnitudes, it would cover effectively the range of possible combinations of initial stresses and strain increments that can be faced in numerical simulation applications.

3.1.2 Step 2: Return mapping

If the trial stress is large enough to cause plastic deformation, the return mapping is solved using a Newton-Raphson algorithm for the computation of the closest point projection from the trial state onto the yield surface.

This will be done by defining two residuals for the model. The first residual is the yield function of the model and the second one, the plastic strain residual:

$$f(\vec{\sigma}) = \varphi(\vec{\sigma}) - \sigma_y \qquad \text{for Hosford Model} \tag{3.3}$$

$$f(\vec{\sigma}) = \left(\sum_{\alpha=0}^{N} \left\langle \frac{\vec{\sigma} \cdot \vec{P}^{\alpha}}{\tau_c^{\alpha}} \right\rangle^{n}\right)^{\frac{1}{n}} - 1 \qquad \text{for Crystal plasticity Model} \tag{3.4}$$

$$\vec{r}(\vec{\sigma}, \Delta\lambda) = -\Delta\vec{\varepsilon}_p(\vec{\sigma}) + \Delta\lambda \frac{\partial f}{\partial \vec{\sigma}} \tag{3.5}$$

Where $\Delta\vec{\varepsilon}_p$ is the plastic strain increment and $\Delta\lambda$ is the incremental consistency parameter.

For Hosford mode, from the yield function expression, it can be concluded that $\frac{\partial \mathrm{f}}{\partial \vec{\sigma}} = \frac{\partial \varphi}{\partial \vec{\sigma}}$.

These two residuals will define a measure of convergence as:

$$\psi = \frac{1}{2}\left[\vec{r} \cdot \vec{r} + \left(\frac{f}{2G}\right)^2\right] \qquad \text{for Hosford Model} \tag{3.6}$$

$$\psi = \frac{1}{2}[\vec{r} \cdot \vec{r} + f^2] \qquad \text{for Crystal plasticity Model} \tag{3.7}$$

For the Hosford Model, shear modulus (G) is used for scaling the yield function and therefore the convergence parameter ψ will be dimensionless. The acceptable solution should result in a convergence parameter, less than a specified threshold. In other words, the iterative algorithm should continue until finding a $\vec{\sigma}$ and $\Delta\lambda$ that makes both residuals small enough. To fulfill this aim, after each iteration, the stress and consistency parameter will be updated using their incremental values. After iteration *k*:

$$\vec{\sigma}_{k+1} = \vec{\sigma}_k + \Delta\vec{\sigma} \tag{3.8}$$

$$\Delta\lambda_{k+1} = \Delta\lambda_k + \Delta(\Delta\lambda) \tag{3.9}$$

Where $\Delta\vec{\sigma}$ is the amount of change in the stress and $\Delta(\Delta\lambda)$, change in incremental consistency parameter in step *k*, and are to be found for each increment having the Hessian matrix of the return mapping algorithm:

$$\boldsymbol{H}_k^{-1} = \boldsymbol{C}^{-1} + \Delta\lambda_k \frac{\partial^2 f_k}{\partial\vec{\sigma}\,\partial\vec{\sigma}} \tag{3.10}$$

The incremental values will then can be obtained by the following equations:

$$\Delta(\Delta\lambda) = \frac{f_k - \vec{r}_k \cdot \boldsymbol{H}_k \cdot \frac{\partial f_k}{\partial\vec{\sigma}}}{\frac{\partial f_k}{\partial\vec{\sigma}} \cdot \boldsymbol{H}_k \cdot \frac{\partial f_k}{\partial\vec{\sigma}}} \tag{3.11}$$

$$\Delta\vec{\sigma} = -\boldsymbol{H}_k \cdot \left(\vec{r}_k + \Delta(\Delta\lambda)\frac{\partial f_k}{\partial\vec{\sigma}}\right) \tag{3.12}$$

Having the stress increment, plastic strain increment used in the plastic strain residual can also be calculated by:

$$\Delta\vec{\varepsilon}_p^{k+1} = \Delta\vec{\varepsilon}_p^{k} - \boldsymbol{C}^{-1} \cdot \Delta\vec{\sigma} \tag{3.13}$$

After each iteration, the value of residuals and then the convergence measure ψ will be calculated. For the Hosford model, if this parameter is less than a defined tolerance say ψ_{limit}, the solution will be recognized as converged. For the crystal plasticity model, however, both the yield function and plastic residual are checked to make sure both the residuals are smaller than defined limit values.

the flowchart of such a routine is summarized in the figure below:

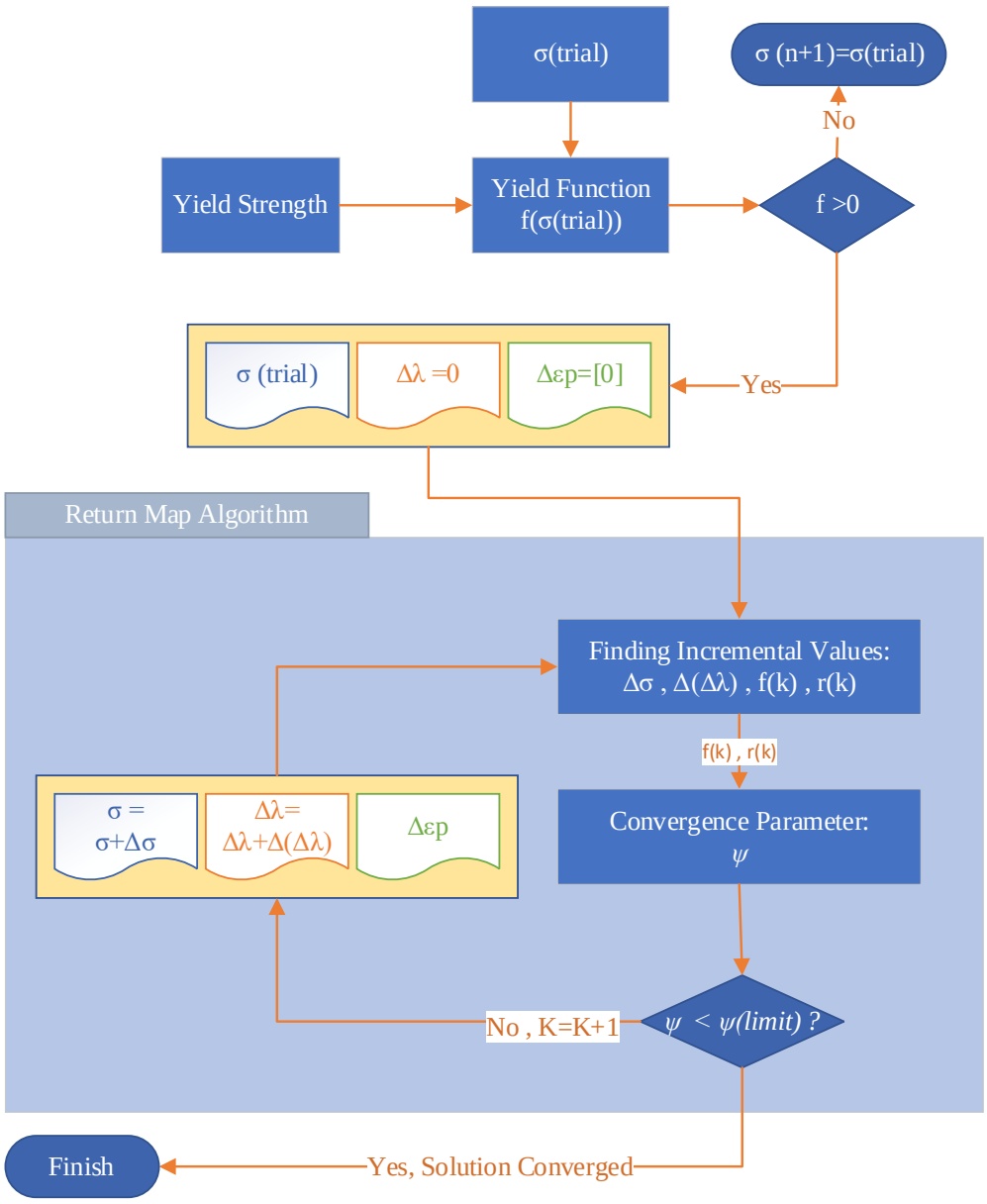

Figure 4- the overview of the return mapping algorithm

3.2 Line search modification

In this section, the implementation of a line search modification for improving the effectiveness of the return mapping algorithm using Newton-Raphson is discussed. Results and effectiveness of line search modification will be discussed in the next chapter.

Line search adds one simple step to the Newton-Raphson method. By defining a new variable denoted as α here, it tries to modify the direction of search found by the Newton algorithm by reducing the step size of each iteration, if necessary. This modification is based on the idea that there might be a solution where only a fraction (α) of the incremental values ($\Delta\vec{\sigma}$ and $\Delta(\Delta\lambda)$) are used in each step and then that step might take the variables closer to the final solution than the condition where whole the incremental values are used for updating the stress and strain variables. As mentioned before, the convergency parameter ψ is used as the measure of improvement of the solution in each step and therefore can serve as the merit function of the line search as well. By introducing the line search modification, equations 3.8 and 3.9 will be modified as:

$$\vec{\sigma}_{k+1} = \vec{\sigma}_k + \alpha_k \Delta\overrightarrow{\sigma} \tag{3.14}$$

$$\Delta\lambda_{k+1} = \Delta\lambda_k + \alpha_k \Delta(\Delta\lambda) \tag{3.15}$$

Where α_k is the step size and should be found in a way that minimizes the merit function for each step. For step *k*:

$$\psi(\alpha_k) = \frac{1}{2}\left[\vec{r}(\alpha_k)\cdot\overrightarrow{r}(\alpha_k) + \left(\frac{f(\alpha_k)}{2G}\right)^2\right] \qquad \text{for Hosford Model} \tag{3.16}$$

$$\psi(\alpha_k) = \frac{1}{2}[\vec{r}(\alpha_k)\cdot\vec{r}(\alpha_k) + f^2] \qquad \text{for Crystal plasticity Model} \tag{3.17}$$

The main challenge of line search is now to find a reasonable value of α_k or Newton step size, varying from 0 to 1, that gives enough decrease in the merit function. The $\alpha_k = 1$ condition will be the same as the Newton step, so the residuals will be calculated using the whole incremental values whereas the $\alpha_k = 0$ is simply evaluating the merit function using the starting residuals for that certain step. Finding merit function for any other α value comes with

some computational cost so determining the actual α value that minimizes the merit function is a difficult problem. One idea is to rely on a proper approximation that makes merit function sufficiently small in each step instead of trying to find the exact minimum point. Since $\psi'(0) = -2\psi(0)$ for this case The quadratic approximation is suggested to be one solution [15]:

$$\hat{\psi}(\alpha_k) = (1 - 2\alpha_k + {\alpha_k}^2)\psi(0) + {\alpha_k}^2\psi(1) \qquad (3.18)$$

Where $\hat{\psi}(\alpha_k)$ is a quadratic approximation to $\psi(\alpha_k)$ and the value of α_k that minimizes the approximation is:

$$\alpha_k = \frac{\psi(0)}{\psi(1) + \psi(0)} \qquad (3.19)$$

Having the residuals before each Newton step as well as the results of the Newton-Raphson solution algorithm, $\psi(0)$ and $\psi(1)$ can be easily obtained without extra computational cost. Next is to check if such α_k results in a sufficient decrease in the merit function, and otherwise, α should be found in an iterative solution denoted with *j*:

$$\alpha_k^{j+1} = \frac{\left(\alpha_k^j\right)^2 \psi(0)}{\psi\left(\alpha_k^j\right) - \left(1 - 2\alpha_k^j\right)\psi(0)} \qquad (3.20)$$

After each *j* iteration, the new α will be used to obtain the merit function using equations 3.16 and 3.17 and if the solution meets the following condition known as the Goldstein's condition [16], such α will be said to be a proper approximation and will be used for modifying the Newton step. If the algorithm can not find such value of α that can satisfy this condition after a determined maximum number of j iterations, the last value will be used.

$$\psi_k^{j+1} < \left(1 - 2\beta\alpha_k^j\right)\psi(0)_k \qquad (3.21)$$

Another condition should be defined to avoid choosing very small α values since it will result in an overall high number of return mapping iterations. So, if α_k^{j+1} is smaller than a certain fraction of α_k^j , denoted as η, $\eta\ \alpha_k^j$ will be chosen to be the new value of α. The parameters β and η are chosen as suggested by the literature [15], $\beta = 10^{-4}$ and η =0.1

The figure below illustrates the flowchart of a return mapping algorithm, modified with a line search technique.

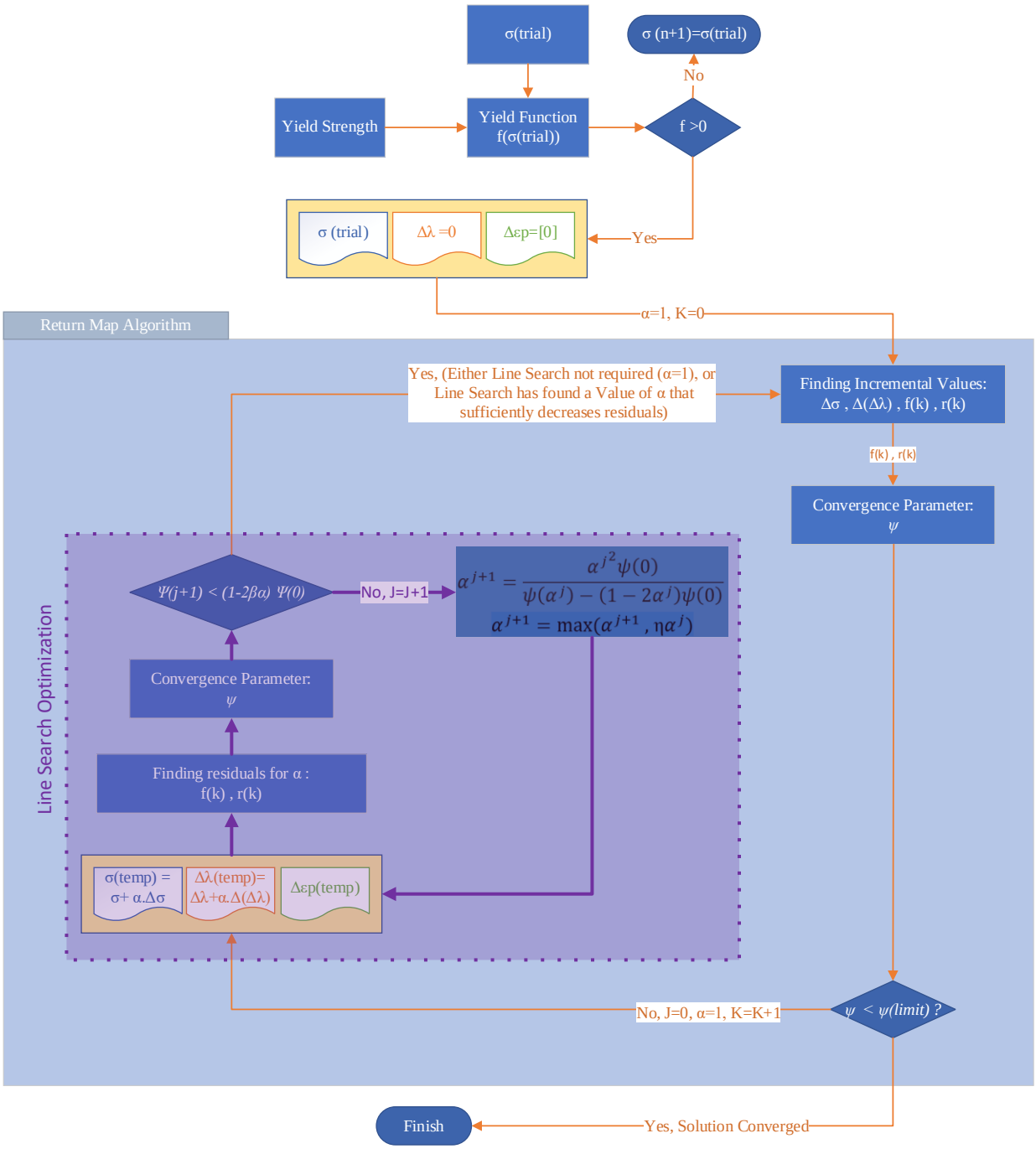

Figure 5-Return mapping algorithm with line search optimization

3.3 Projecting the trial stress

In addition, an effort has been made to improve the convergence speed of the solution by projecting the initial trial stress onto the yield surface and using this projected stress as the starting guess point of the iterations to find the solution.

The projection is performed using equations 3.22 and 3.23 for the Hosford continuum model and crystal plasticity model, respectively:

$$\vec{\sigma}^{\text{trial}}_{\text{projected}} = \frac{\sigma_y \, \vec{\sigma}^{\text{trial}}}{f(\vec{\sigma}) + \sigma_y} \tag{3.22}$$

$$\vec{\sigma}^{\text{trial}}_{\text{projected}} = \frac{\vec{\sigma}^{\text{trial}}}{f(\vec{\sigma}) + 1} \tag{3.23}$$

Such operation will update the initial plastic strain increment and incremental consistency parameter accordingly. Using the projected stress state, these initial guesses will be obtained using the following equations:

$$\Delta\vec{\varepsilon}_p = -\left(\mathbf{C}^{-1} \cdot \left(\vec{\sigma}^{\text{trial}}_{\text{projected}} - \vec{\sigma}^{\text{trial}}\right)\right) \tag{3.24}$$

$$\Delta\lambda = \Delta\vec{\varepsilon}_p \cdot \vec{\sigma}^{\text{trial}}_{\text{projected}} / \sigma_y \qquad \text{for Hosford model} \tag{3.25}$$

$$\Delta\lambda = \Delta\vec{\varepsilon}_p \cdot \vec{\sigma}^{\text{trial}}_{\text{projected}} \qquad \text{for Crystal plasticity model} \tag{3.26}$$

3.4 Parameters of the models

The parameters used in this study are presented in the following table.

General Parameters	
Elastic Module, E	72000 MPa
Poisson's ratio, ν	0.33
Yield Strength, σ_o or σ_y	200 MPa
Line Search Parameter, β	10^{-4}
Line Search Parameter, η	0.1
Maximum number of line search iterations, J_{max}	5
For the Continuum model	
Merit function tolerance, ψ_{limit}	10^{-15}
For the Crystal plasticity model	
Critical resolved shear stress, same for all slip systems	12.9 MPa
Yield residual limit	10^{-8}
Plastic strain residual limit	10^{-20}
C_{11}	106.75 GPa
C_{12}	60.41 GPa
C_{44}	28.34 GPa

Table 3- values used for the parameters of the models and algorithms

For the Hosford Model, the isotropic stiffness tensor is defined using Lame constants as followed [17]:

$$\lambda = \frac{E\nu}{(1+\nu)(1-2\nu)} \quad , \quad \mu = G = \frac{E}{2(1+\nu)}$$

$$\mathbf{C} = \begin{pmatrix} \lambda+2\mu & \lambda & \lambda & 0 & 0 & 0 \\ \lambda & \lambda+2\mu & \lambda & 0 & 0 & 0 \\ \lambda & \lambda & \lambda+2\mu & 0 & 0 & 0 \\ 0 & 0 & 0 & \mu & 0 & 0 \\ 0 & 0 & 0 & 0 & \mu & 0 \\ 0 & 0 & 0 & 0 & 0 & \mu \end{pmatrix}$$

For the crystal plasticity model, due to the cubic symmetry of the FCC aluminum, the constitutive law can be parameterized by only 3 material constants and therefore the stiffness tensor can be written as: [1]

$$\mathbf{C} = \begin{pmatrix} C_{11} & C_{12} & C_{12} & 0 & 0 & 0 \\ C_{12} & C_{11} & C_{12} & 0 & 0 & 0 \\ C_{12} & C_{12} & C_{11} & 0 & 0 & 0 \\ 0 & 0 & 0 & C_{44} & 0 & 0 \\ 0 & 0 & 0 & 0 & C_{44} & 0 \\ 0 & 0 & 0 & 0 & 0 & C_{44} \end{pmatrix}$$

The material parameters used in this study are the constants given for the AA 1050 alloys in literature. [18]

4 Results

The return mapping algorithm along with the modifications presented in the previous chapter is implemented in a python 3.7 code. This chapter is divided into two main sections presenting the results generated by two models discussed in this work: continuum plasticity isotropic Hosford model, and rate-independent crystal plasticity model. Each model is tested with feeding two sets of stress states as the trial stress. The first set of stresses are chosen so that they uniformly cover the π-plane (for Hosford model) or the $\sigma_{11} - \sigma_{22}$ plane (for crystal plasticity model) as a section of the whole stress space. This is chosen so that the results can be compared with the results published by Scherzinger (2016) in a paper investigating the implementation of the line search algorithm for the Hosford yield surface. [7]

However, to evaluate the efficiency of the algorithm for the crystal plasticity model, one must analyze such a set that effectively covers all possible stress states, including those with shear components. To this end, another set with 10,000 stress states, uniformly distributed in 5-dimensional stress space is used. To capture the effect of stress state magnitude, seven iso-potential layers are given to each model. Each layer is populated with stress states obtained with multiplying stress tensors with a factor to generate trial stresses with $\sigma_{\text{von Mises}}/\sigma_0$ (for Hosford model) or yield function (for crystal plasticity model) in the range of [2,5,10,15,20,25,30].

To be able to evaluate the effect of line search and projection modifications, separately and together, four different settings are used for each run, along with a case name to denote each setting, as described in the following table.

Case	Line Search	Trial stress projection
L1_P1	✓	✓
L1_P0	✓	×
L0_P1	×	✓
L0_P0	×	×

Table 4- Different configurations used for analyzing the models

The number of iterations for each trail stress along with the final converged stress tensor is recorded. moreover, the value of merit function, as well as two other residuals and the obtained stress state in each return mapping step, are stored.

No hardening model is implemented and both of the models are considering perfect plasticity to be the case.

4.1 Continuum Plasticity Hosford Model

The effectiveness of the modifications is tested by running the algorithm for Hosford Model with the exponents of a = 4, 6, 8, and 100. To evaluate the convergence behavior of different trial stress states in the π-plane, outside of yield surface with von Misses stress up to 30 times the yield strength, a color-coded map is used where colors represent the number of iterations for each stress state. Nearly 100,000 stress states are analyzed for generating each graph.

In addition, the shape of the yield surface obtained using each exponent for the L1_P1 cases are presented.

For the case of a=4, where the obtained yield surface will be a von Mises yield surface, the Newton algorithm reduces to the radial return algorithm. However, with increasing the exponent, the closest point projection problem no longer gives a radial return and in addition to the consistency parameter, plastic flow direction should be determined in each iteration. Exponents 6 and 8 have shown to be a proper choice for modeling BCC and FCC structures, respectively. [19] Exponent 100 represents a yield surface fairly close to the Tresca yield surface and is a good choice to evaluate the reliability of the model implementation when using higher exponents.

For a=4, Fig 6 shows the generated results for the four different configurations that were tested.

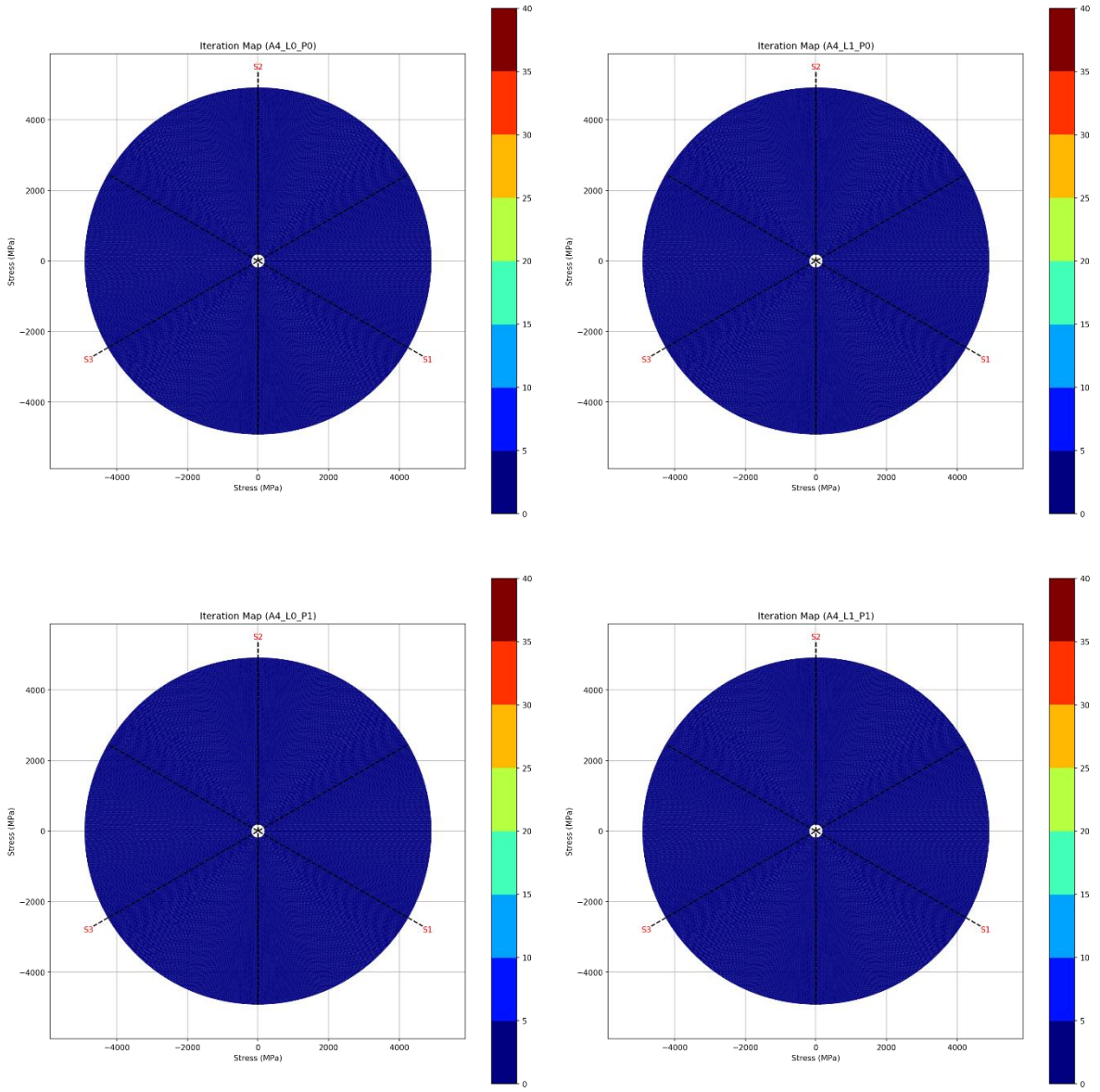

Figure 6 - Iteration Map graphs for Hosford Model, with exponent a=4

As expected, all the trial stress states converge with one iteration for all the cases, however for higher exponents of 6 and 8, return map algorithm with Newton-Raphson solution, fails to have all the stress states converged within iteration numbers less than 40, as shown in Figures 7 and 8, respectively.

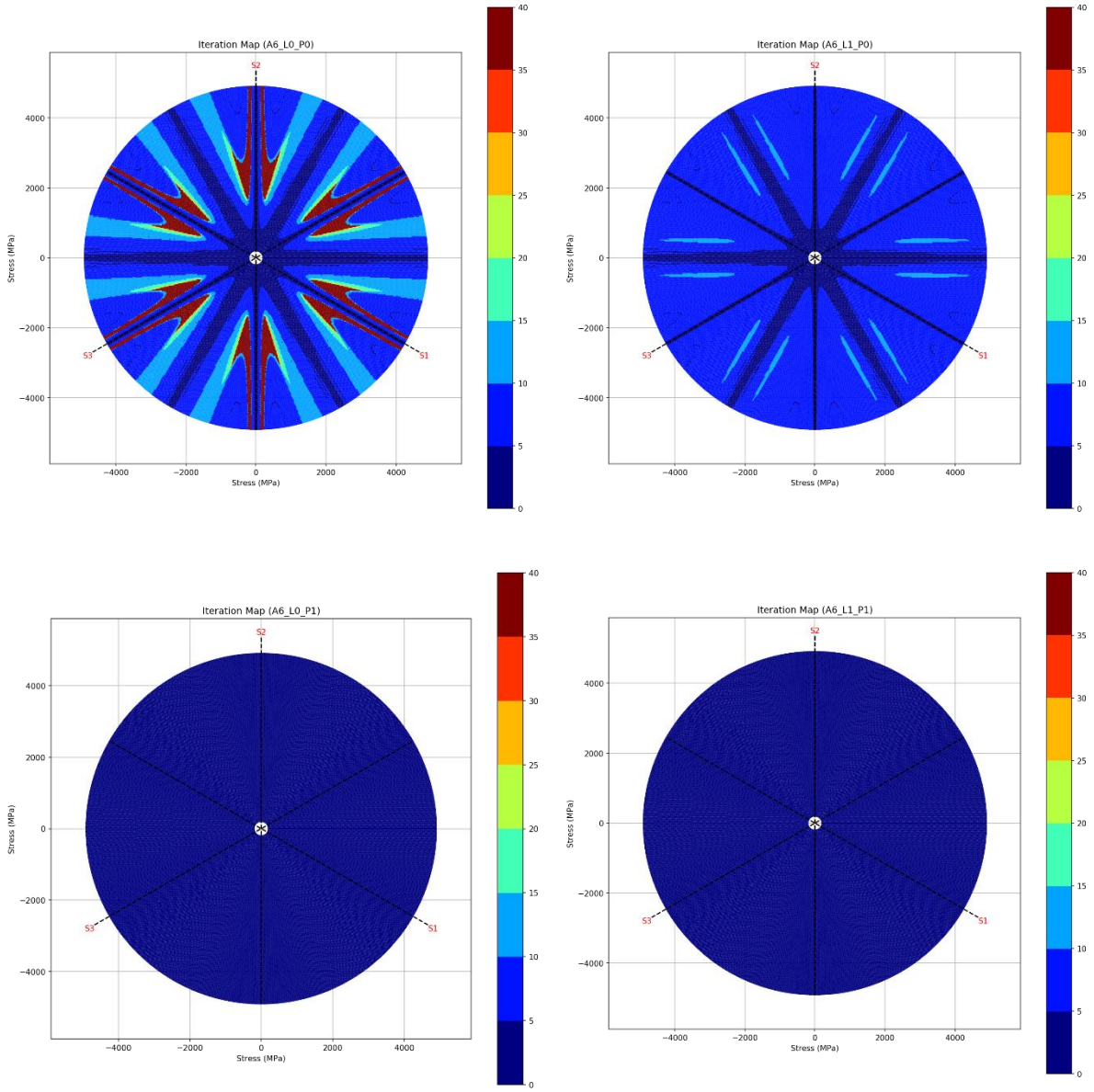

Figure 7- Iteration Map graphs for Hosford Model, with exponent a=6

For exponent 6, the Newton-Raphson solution fails to converge 8.8% of the given trial stresses in less than 40 iterations. With increasing the exponent to 8, the failed portion increases to 52.5%. Implementing the line search is proven to considerably improve convergence behavior in both of these cases, resulting in full convergency for the set of analyzed stress states. Projecting trial stresses to the yield surface before performing the return map, results in yet

more improvement such that even without line search optimization, all the trial stresses converge in less than 4 iterations for a=6 and 6 iterations for the a=8 case.

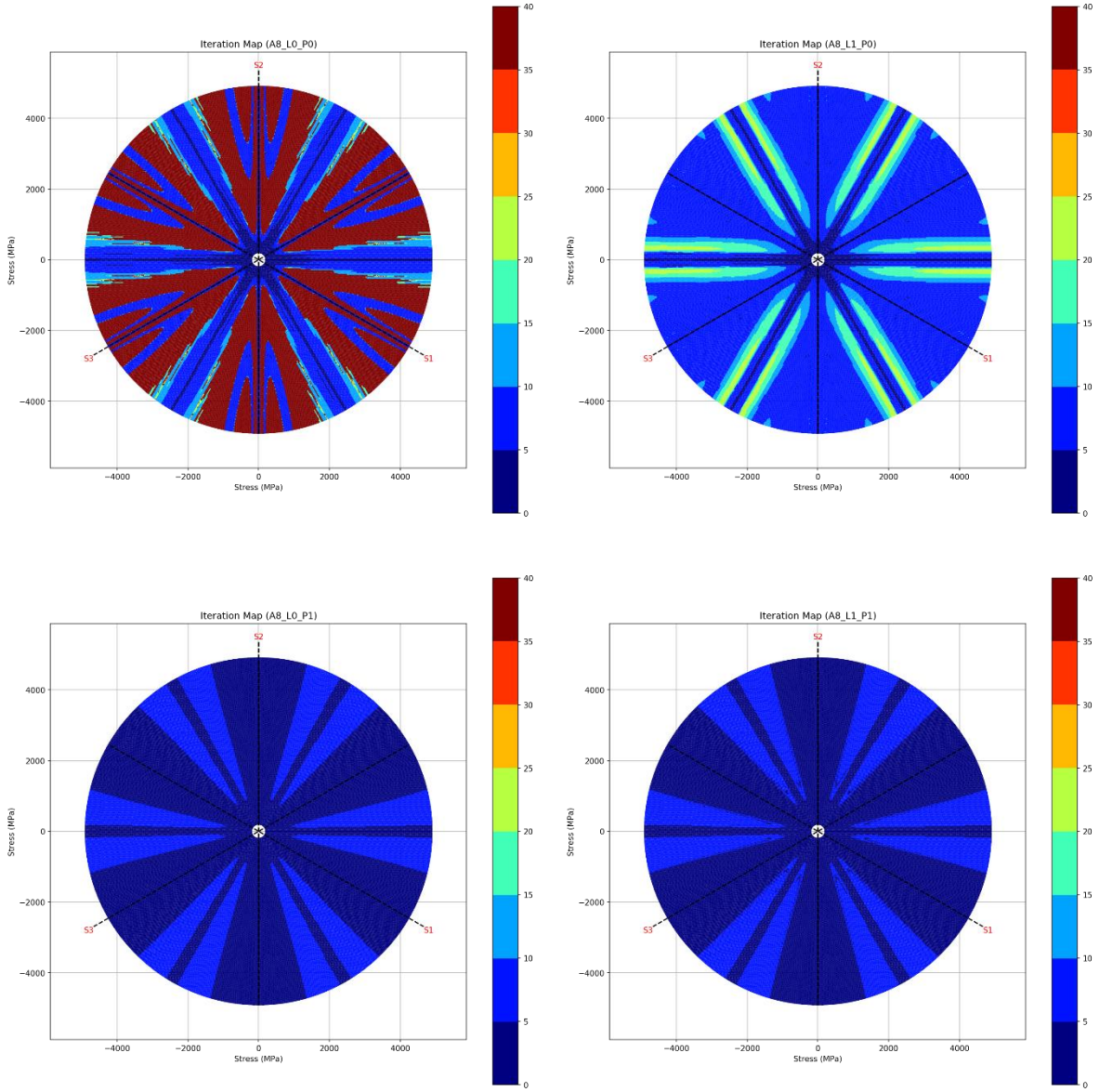

Figure 8- Iteration Map graphs for Hosford Model, with exponent a=8

Testing the algorithm on the extreme case of a=100 emphasizes the improvement that is achievable by modifying the return map to include a line search, as shown in figure 9. However, starting from projected trial stress doesn't seem to give much improvement without the line search, as both cases fail to converge %88 and %92 of the tested trial stresses, with and without trial stress projection modification, respectively. On the other hand, the expansion of

the area with darker blue shades shows that projection modification accelerates the convergence process when the line search is employed.

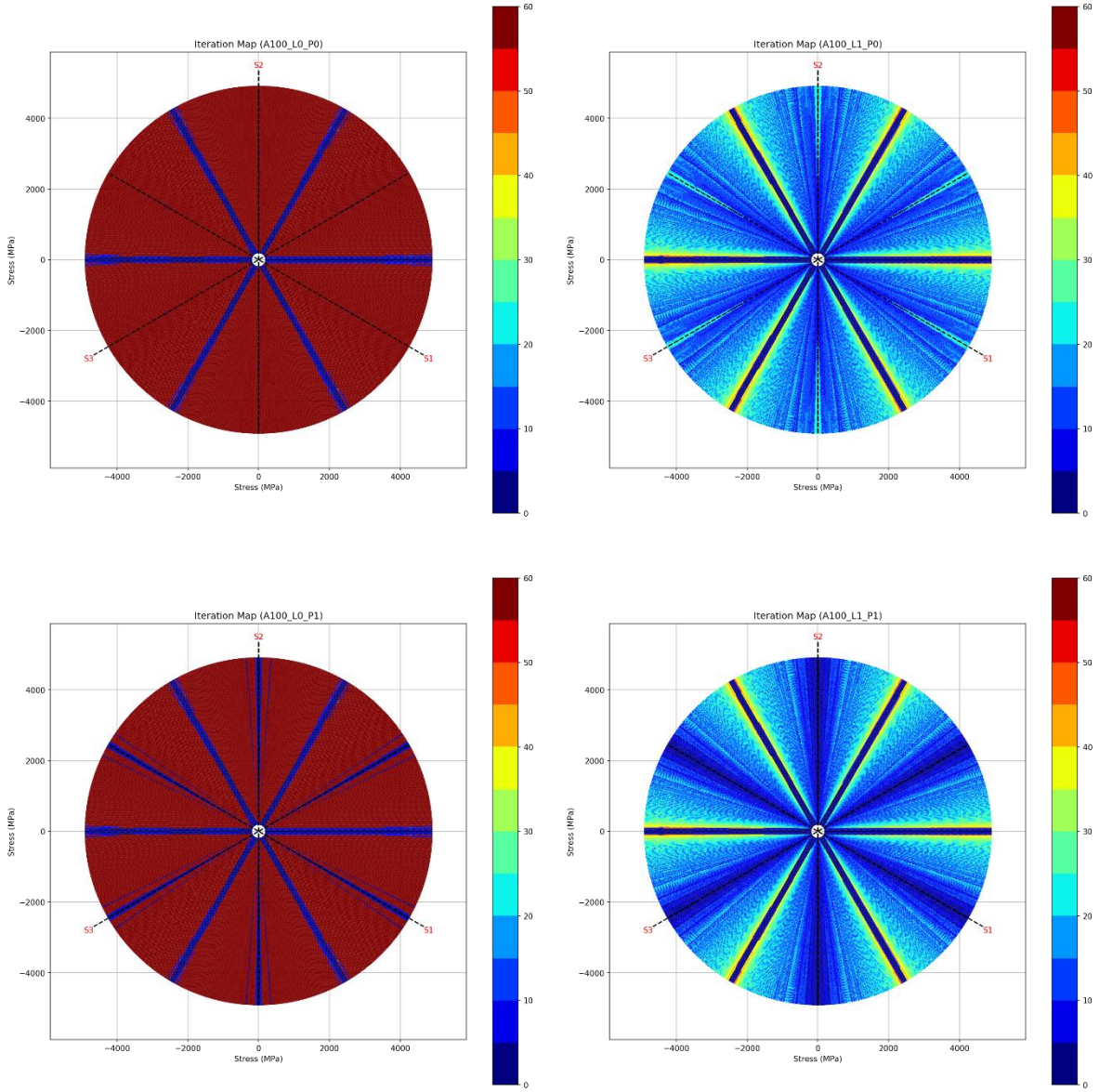

Figure 9- Iteration Map graphs for Hosford Model, with exponent a=100

For the exponents of 6, 8 and100, results for the pure Newton-Raphson return map and line search modification can be compared with the plots generated by Scherzinger (2016), as presented in figure 10. This comparison validates the accuracy and reliability of the python code tool developed for this work.

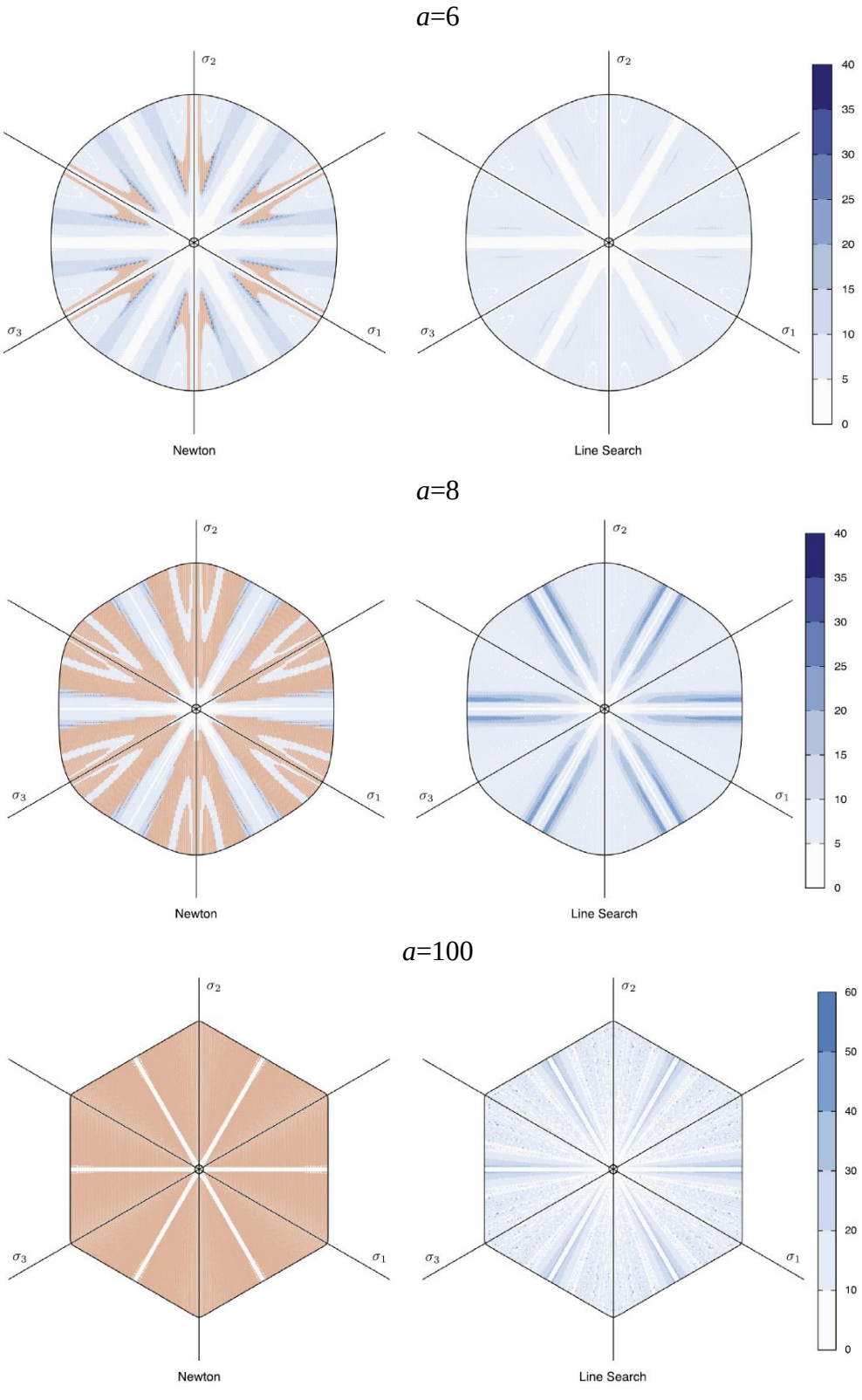

Figure 10- Comparison of the Newton algorithm and the line search algorithm for the Hosford model with a=6,8,100 [7]

Figure 11 shows the yield surfaces generated by the algorithm for different exponents, using the L1_P1 setting where all the tested trial stresses are successfully converged. As expected, a=4 which indicates the von Mises yield surface with a circular cylinder with the axis along the hydrostatic axis makes a full circle when projected on the π-plane. With Increasing the exponent, the curvature increases near to the principal stress axes and for a=100 the result is very similar to the π-plane section of the Tresca hexagonal cylinder.

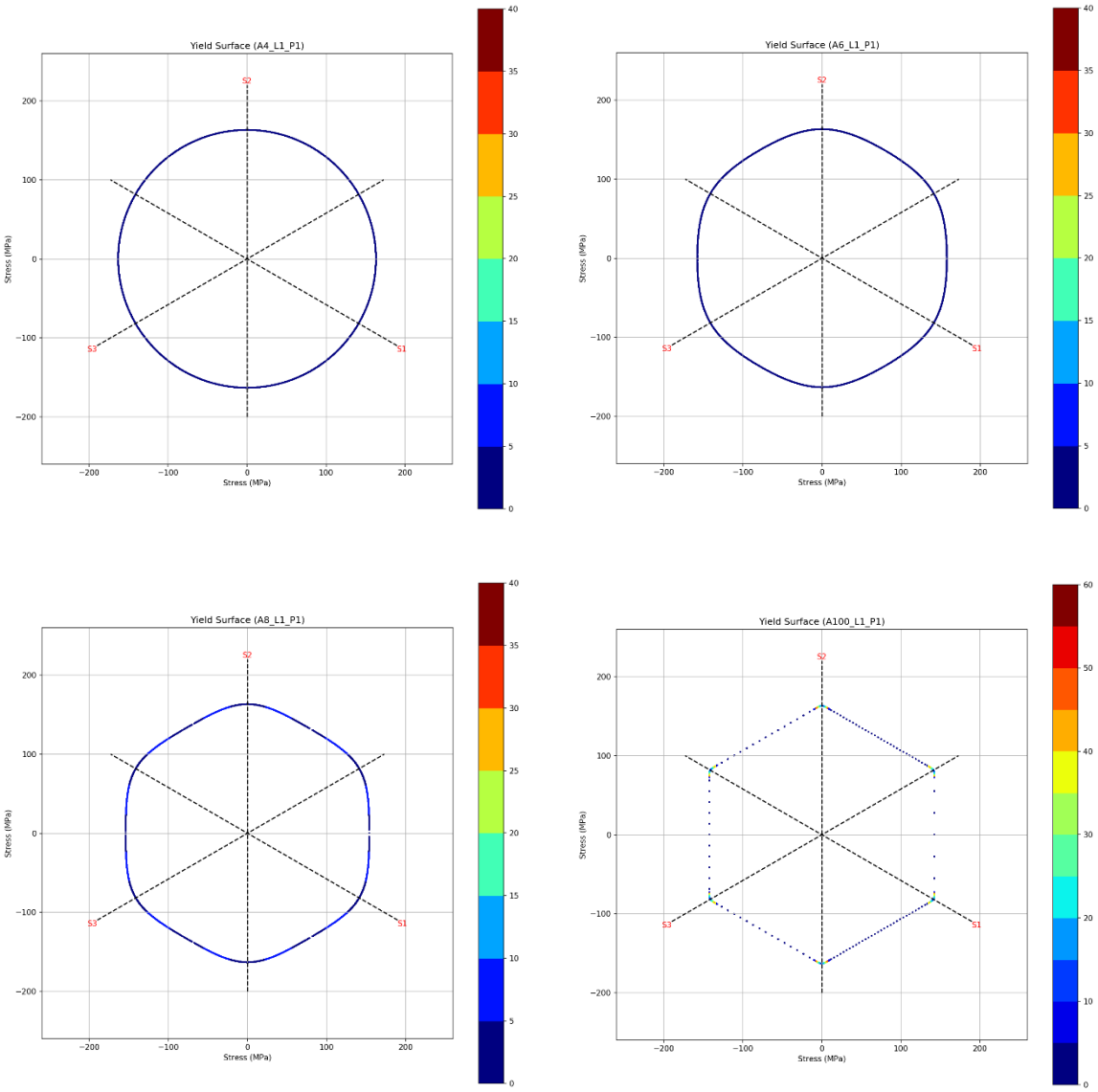

Figure 11- The generated yield surfaces with different exponents for L1_P1 configuration

The next step is to test the algorithm with the set of trial stresses including full tensor components. Instead of return map plots, the results of this part are presented as histograms showing the iteration distributions for each case.

First, stress state tensors are analyzed with the Newton-Raphson algorithm. The portion of stress states that didn't converge after 60 iterations are measured and presented in figure 12. Only for the von Mises (a=4) case, all the points converge unconditionally. With increasing the exponent, the portion of unconverged points increases, up to %78 for the a=100 case. Using projection modification improves convergency for exponents 6 and 8, yet it doesn't have a considerable effect on a=100 case, with the maximum allowed iteration of 60. The same behavior is observed when looking at the π-plane iteration maps for these exponents.

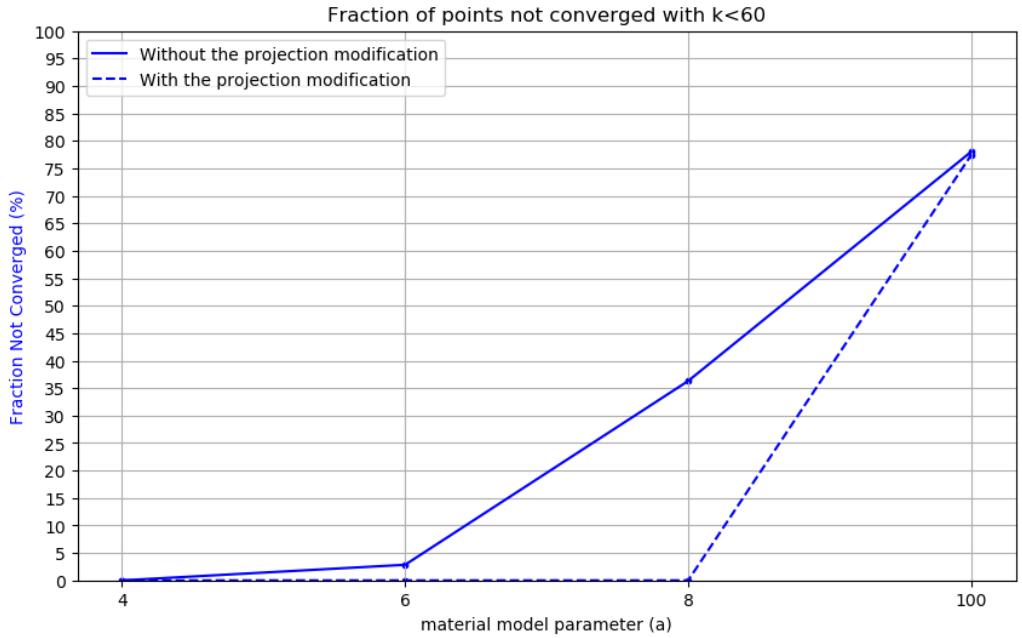

Figure 12- Convergence behavior of the algorithm for the Hosford model, without line search modification, for different exponents.

The effectiveness of the projection modification when using the exponents 6 and 8 is more clear when plotting the iteration distribution curves for each case. As shown in figure 13, when using the projected stress states as the starting point of the solution, all of the analyzed points converge in less than 6 iterations whereas the same curves without projection modification are broader and even some portion of the points fail to converge within the limited number of iterations.

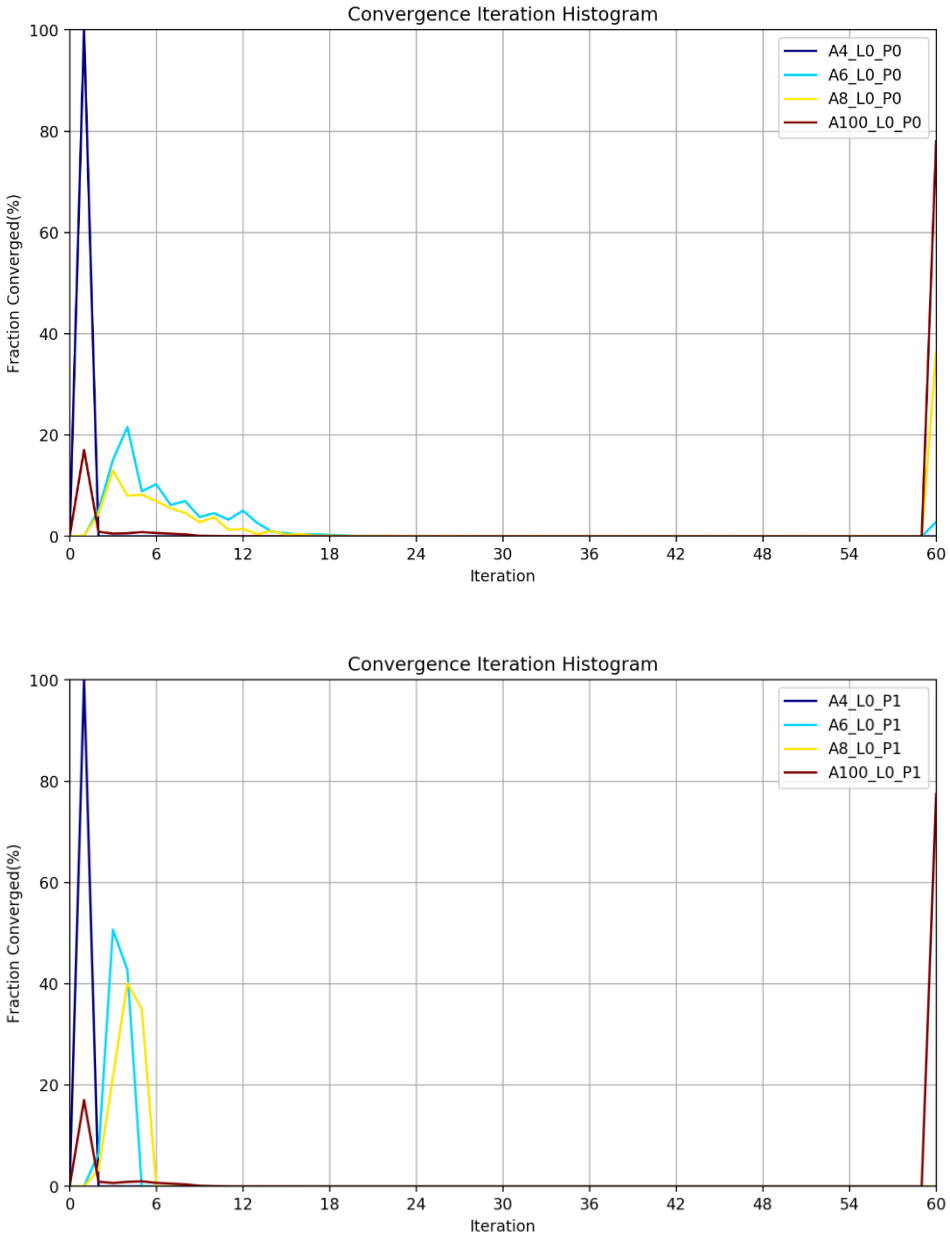

Figure 13- Distribution of the number of iterations for the Hosford model for different cases without line search modification

Same as the results observed for the first set of points (tensors without off-diagonal components), applying line search modification dramatically improves the convergence behavior. The results approve that it is possible to achieve %100 convergence for the analyzed sets with and without projection modification. Iteration distribution graphs give a clear overview of the results, as shown in figure 14.

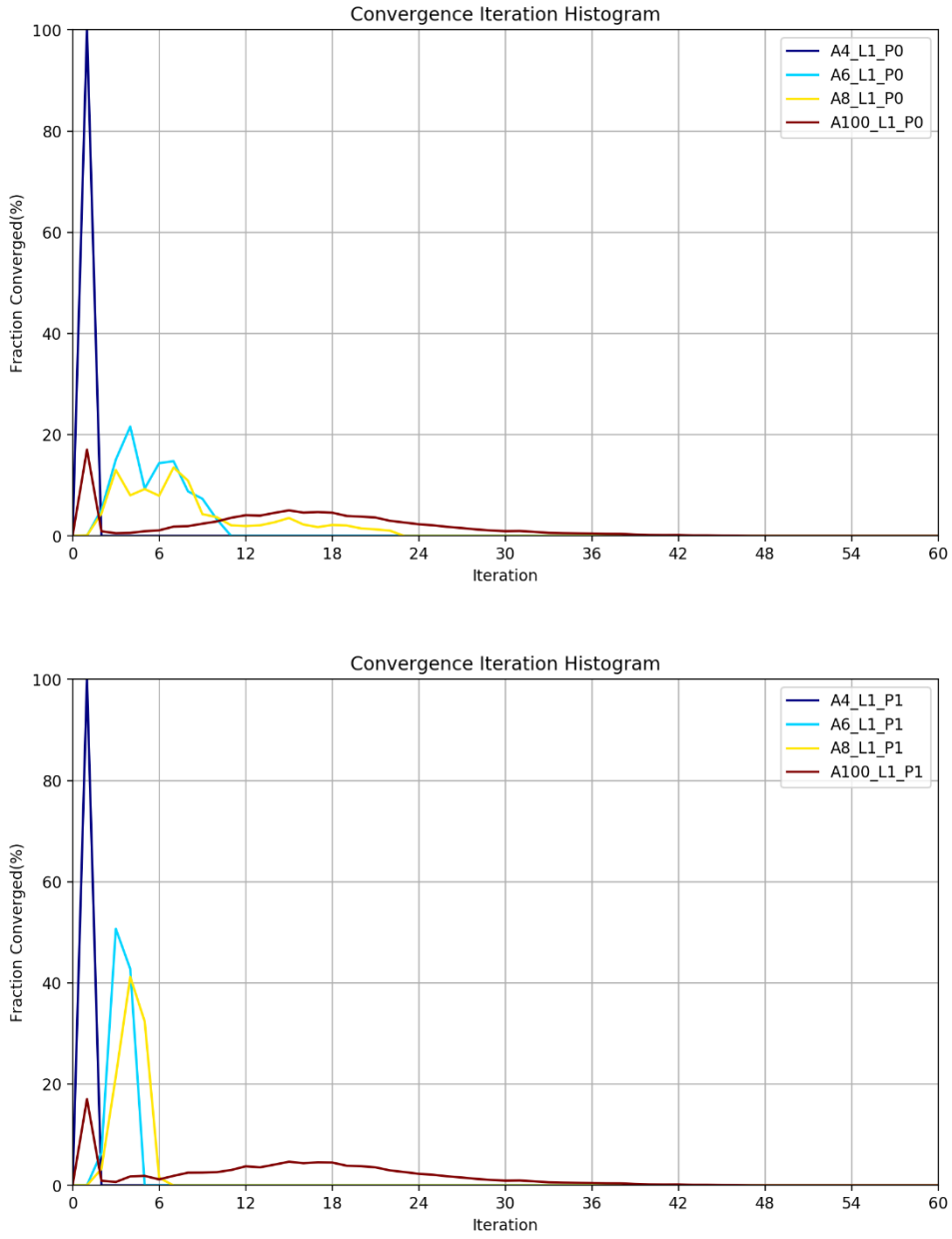

Figure 14- Distribution of the number of iterations for the Hosford Model for different cases with line search modification

With Increasing the exponent n, iteration distribution curves broaden, increasing the average iteration for convergence for higher exponents. However, even for the case of a=100, there is a certain portion of points (possibly the ones that can converge with a simple radial return) that converge in less than three iterations. For a=6 and 8, Using the projected stress states effectively pushes the curves towards lower iterations, creating sharp peaks where the majority of the points converge with almost the same iterations. This is better shown in figure 15, demonstrating the number of iterations where a certain portion of stress states from the tested

set are converged. With the projection modification applied, the slope of lines is decreased to almost zero for exponents less than 8, meaning such cases have almost the same convergence behavior.

a) Without projection modification

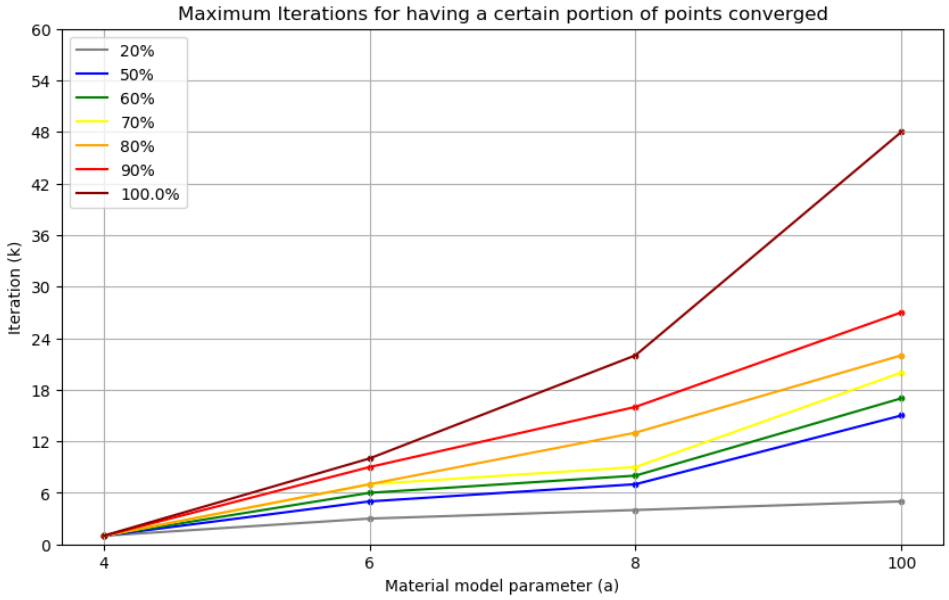

b) With projection modification

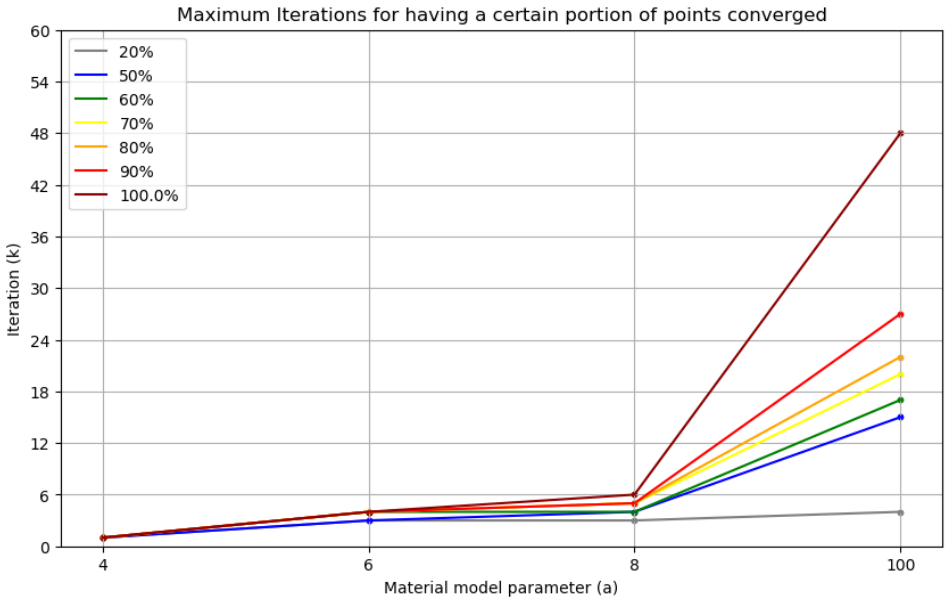

Figure 15- The number of iterations that take to have a certain portion of stress tensors from the set converged when line search modification is applied.

In the case of the Hosford model, the π-plane set of points can correctly present the general behavior of the model. The reason for this is that every trial stress with only the principal components behaves the same as all the other stress states that have the same principal stresses (eigenvalues and vectors), due to the isotopic nature of this model. As shown in figure 16, The results of applying the algorithm on both stress sets were more or less the same because these two sets of points, although including different trail stresses but were large enough to represent the whole space. This is not the case for the crystal plasticity model.

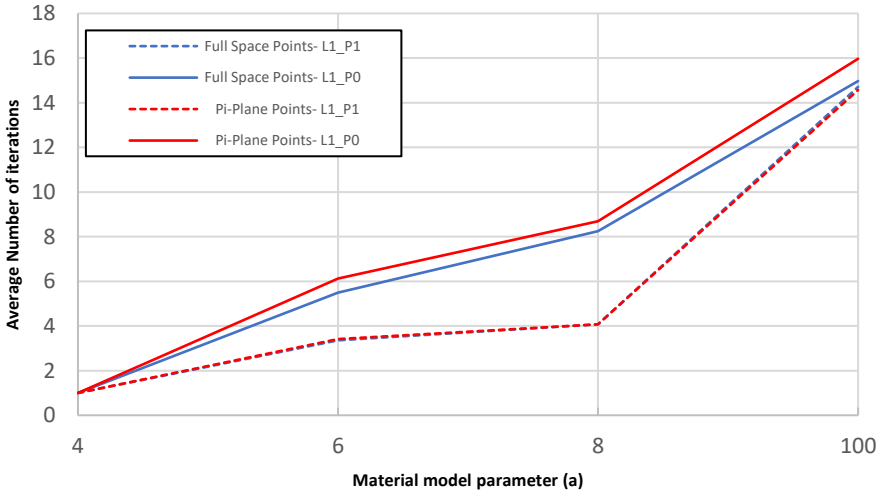

Figure 16- Comparing the results of applying the algorithm on two sets of points, with the line search modification

4.2 Crystal Plasticity Model

The results of applying the discussed modifications on the return mapping algorithm for the crystal plasticity model are presented in this section. Unlike the Hosford model, the results that can be deduced from the analysis of the first set of points ($\sigma_{11} - \sigma_{22}$ plane), can not be generalized due to the anisotropic nature of the crystal plasticity model. The followings are the results of analyzing the set of tensors with full components, as it is more general and comprehensive. The $\sigma_{11} - \sigma_{22}$ plane iteration map plots are presented in Appendix A.

For better understanding the behavior of algorithm and modifications, different cases were tried with the n exponent varying in the range of 20 to 10,000. First, tensors were analyzed using the Newton-Raphson solution, starting with the original as well as projected stress states. As shown in figure 17, the algorithm has a very limited capability, even for the lower exponents in this range. The best achievable result is observed to be for the exponent 20 with projected stress

states, where only 7 percent of the points are converged. For higher exponents, almost no convergence is observed when using full Newton step increments in each iteration.

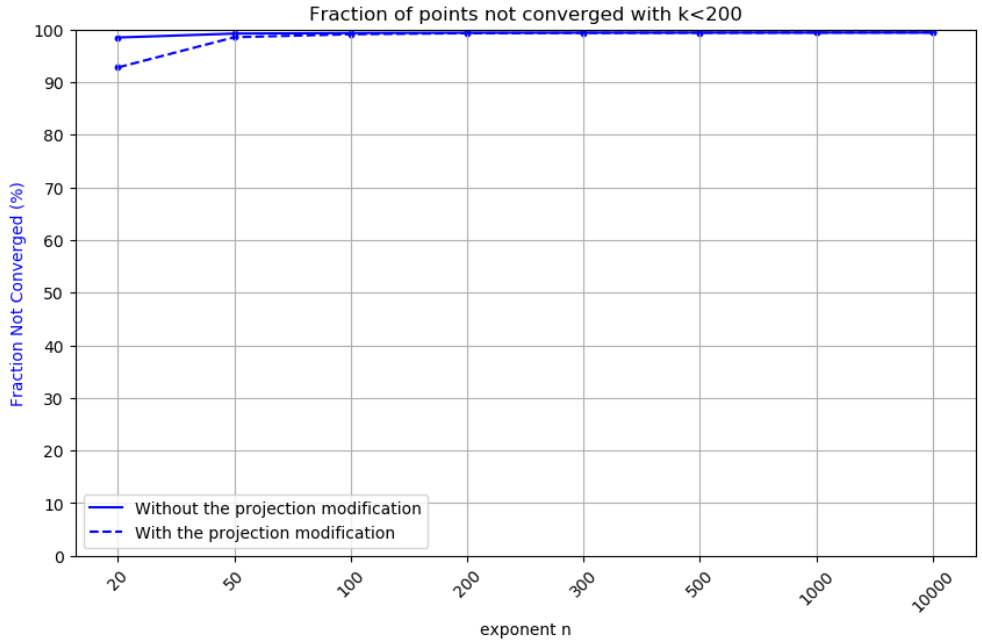

Figure 17- Convergence behavior of the algorithm for the Crystal plasticity model, without line search modification, for different exponents

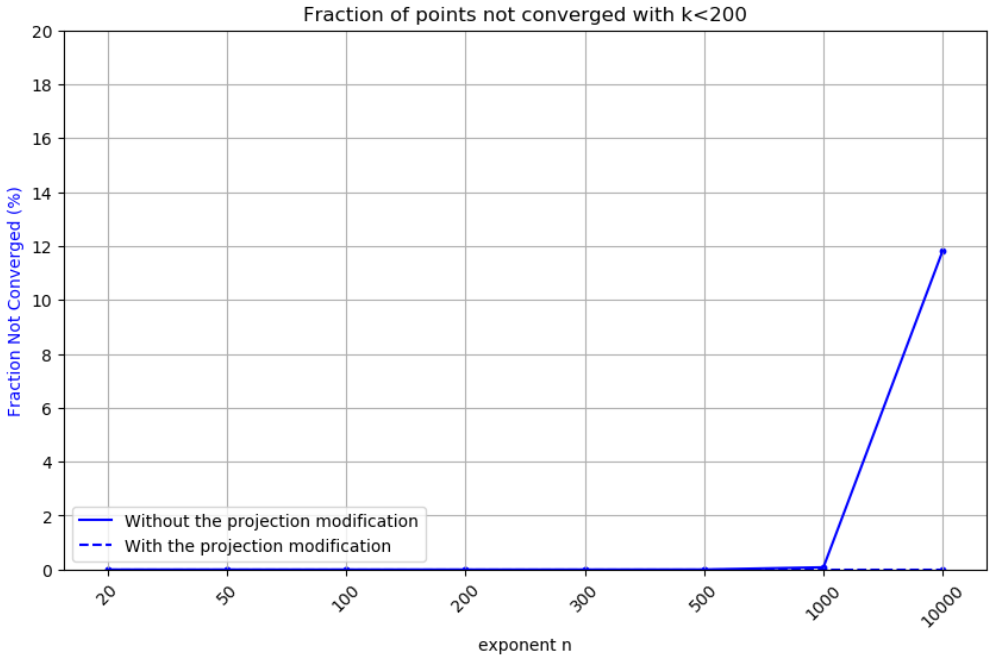

Figure 18- Convergence behavior of the algorithm for the Crystal plasticity model, with line search modification, for different exponents

Same as the results of the continuum model, introducing line search modification demonstrates a significant improvement, as shown in figure 18. Up to n=300, the algorithm is capable of reducing the residuals to the defined limits and finding the converged solution for all the 70,000 tested stress states in the range of f=[2 to 30], with less than 200 iterations. However, by increasing the exponent to n=10,000, a certain portion of the given stress states fail to converge within the limited iterations. Almost %12 of the analyzed set does not converge with $k<200$ which proves that the line search optimization is not sufficiently effective for this case. However, considering the shape of the iteration distribution curve, presented in figure 19, it seems that 200 iteration is simply just not enough, as it is in the broadening range of the curve, and increasing the maximum allowed iterations will have all the stress states converged, eventually.

Achieving %100 convergence for the exponent n=10,000 is possible with much fewer iterations when the return mapping is performed using the projected stress states. As shown in figures 18 and 19, the effect of projection modification is significant, particularly for higher exponents. The distribution curves are narrowed showing a distinct peak. For the case of n=10,000, the peak is decreased from almost 120 to 47.

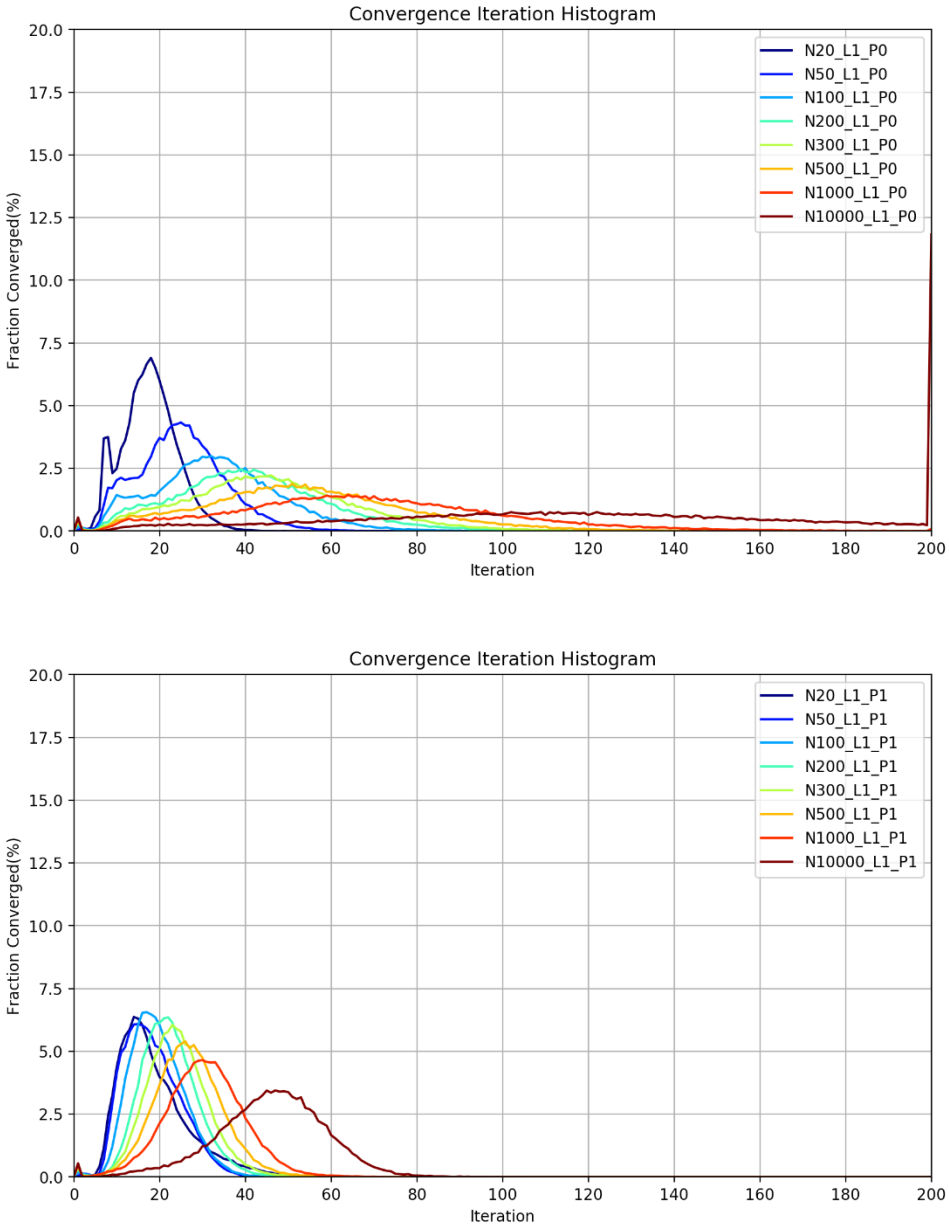

Figure 19- Distribution of the number of iterations for Crystal plasticity model, for different cases with line search modification

Another effect of projection modification can be observed in fig 20 showing the number of iterations for achieving a certain converged portion of points. It seems that the solution is less sensitive to the value of the exponent, allowing the algorithm to handle higher exponents without failure.

a) Without projection modification

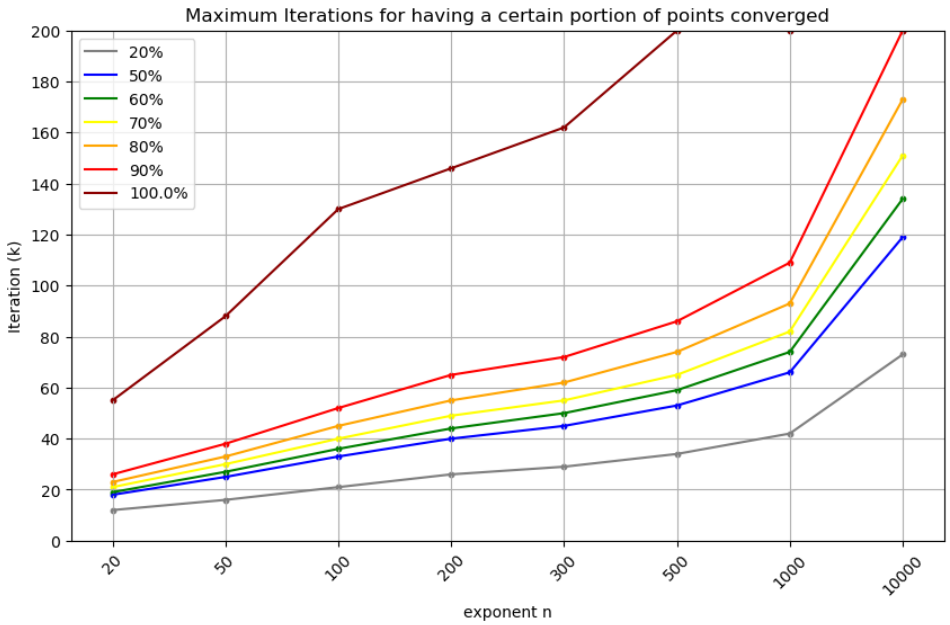

b) With projection modification

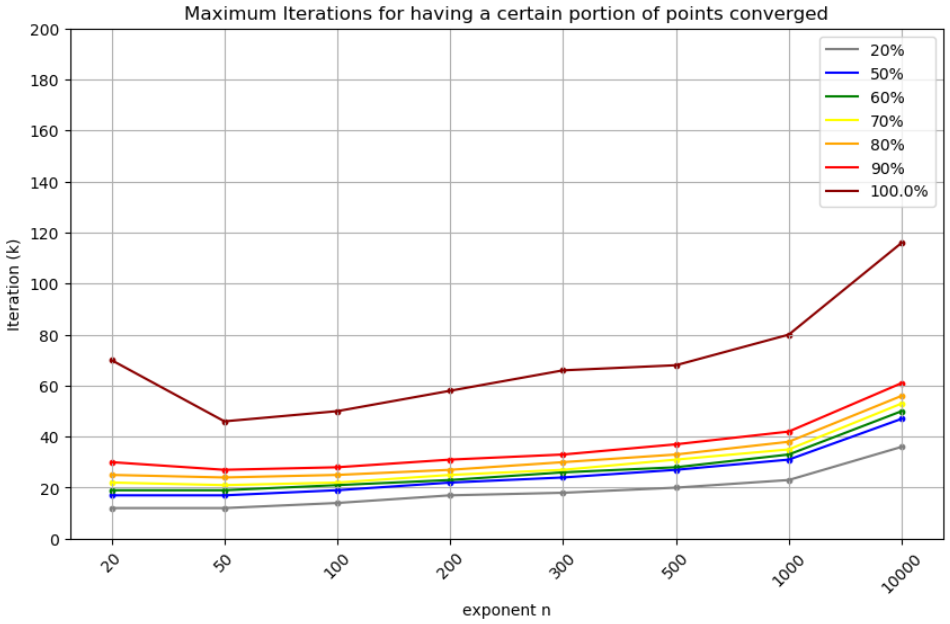

Figure 20- The number of iterations that take to have a certain portion of stress tensors from the set converged when line search modification is applied.

For all the exponents higher than 20, the average number of iterations is decreased by introducing the projection modification. This improvement is more emphasized when using higher exponents as shown in figure 21. For the solution without projection modification, a dotted line is used for exponents higher than 300, because not all the points are converged for these cases and the values do not represent the true average number of "iterations to convergence". With increasing the maximum number of allowed iterations, this part of the line is expected to shift to even higher values, slightly for n=500 and 1000 and considerably for n=10,000, considering their ratio of convergence being %99.99, %99.91 ad %88.2 respectively.

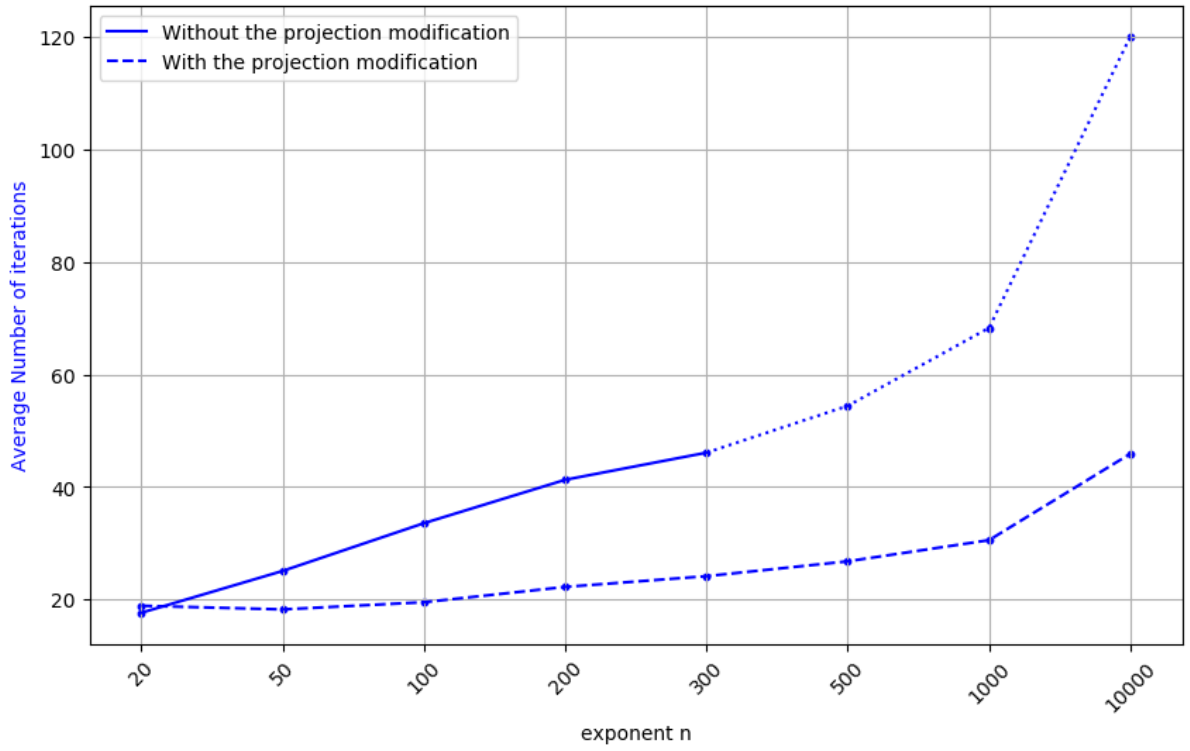

Figure 21- Average number of iterations for convergence for a point, with line search modification for crystal plasticity model

5 Discussion

To understand the mechanism by which, line search and projection modifications improve the effectiveness of the return mapping algorithm solved by the Newton-Raphson method, the following graphs are made, illustrating the path by which the trial stress converges towards the yield surface. In addition, the value of merit function after each step is stored and plotted to demonstrate the alteration of the merit function value as the solution proceeds. The initial stress tensor used for generating the following data is:

$$\vec{\sigma} = [\sigma_{11} \quad \sigma_{22} \quad \sigma_{33} \quad \sigma_{23} \quad \sigma_{13} \quad \sigma_{12}] = [500 \quad 300 \quad -600 \quad 0 \quad 0 \quad 0] \text{ MPa}$$

Hosford model with the exponent of 8 is applied to this stress state. The von mises stress for this case is almost 5 times the yield strength.

5.1 Line search modification

A comparison between the Newton-Raphson algorithm and the line search implemented one is presented in figures 22 and 23. While the Newton algorithm fails to converge this specific trial stress, line search modification successfully converges it in 8 iterations.

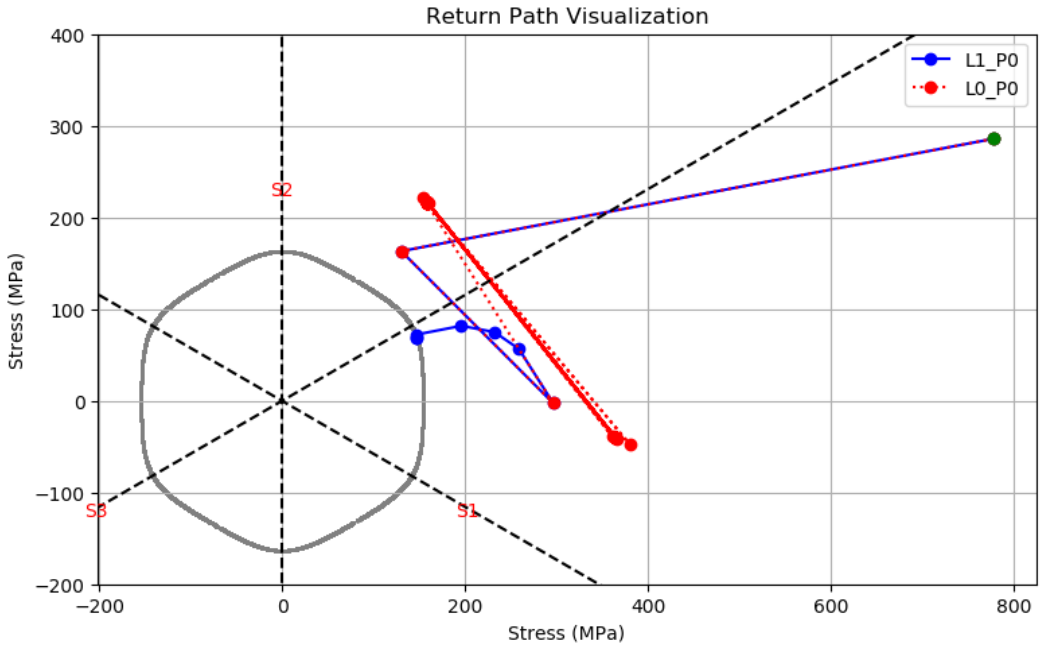

Figure 22- return path visualization for a test tensor. Hosford Model with the exponent of *a*=8 is applied.

Both of the algorithms share the first two steps. Based on the routine described in chapter 3 for line search implementation, this is possible only if the Newton step is able to sufficiently decrease residuals, hence the merit function.

in step 3 however, residuals increase with taking a full Newton step which is reflected as divergence in figure 22. This increase is captured by the algorithm which consequently initiates the line search subroutine. By using α values suggested by the quadratic approximation and search direction found by the Newton algorithm, the next stress, consistency parameter, and plastic strain increment values are computed so that the merit function sufficiently decreases. Eventually, within 8 iterations, this leads to finding such a solution lying on the yield surface that satisfies the defined convergence criterion.

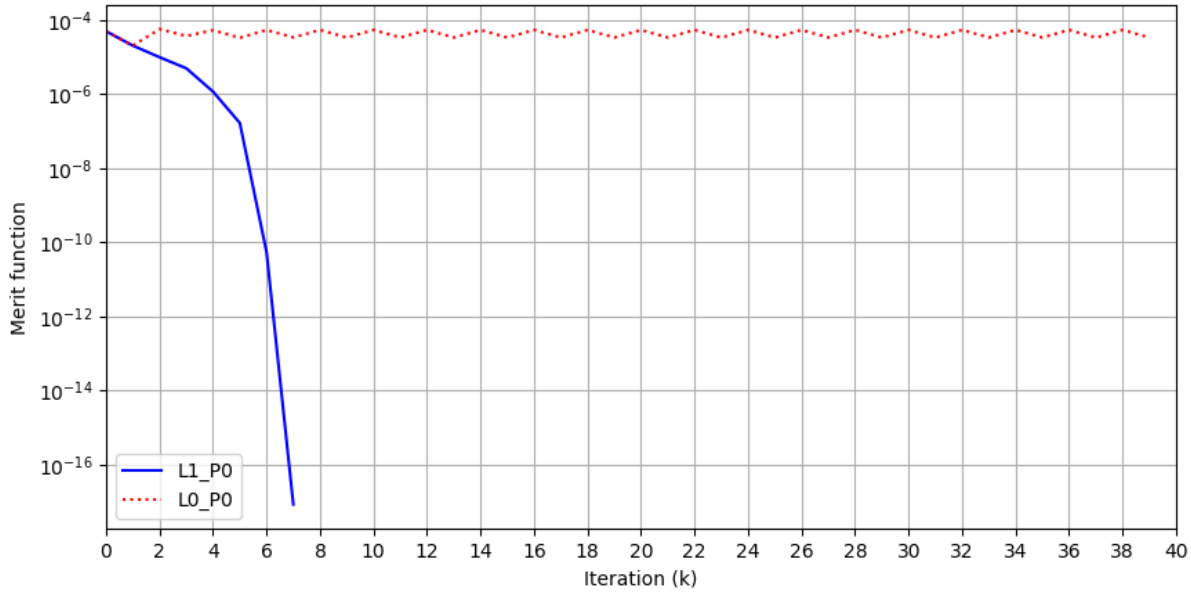

Figure 23- Merit function as a function of iteration count, for Hosford model with the exponent of 8 for a test trial stress state

As described in chapter 3, the line search algorithm uses a quadratic approximation to evaluate the value of α that minimizes the merit function in an iterative solution. Figure 24 provides a graphical explanation of such a procedure, plotted for k=3 using the discussed trial stress tensor. The solid blue line indicates the quadratic approximation with a minimum at α=0.264. To investigate how close this approximation is to the α that will result in maximum achievable improvement, the actual merit function curve is plotted alongside. Even though the approximation doesn't accurately detect the best possible value for α, but by decreasing the

merit function from almost 2.8 times its value before taking step *k*=3, to almost half of that, it leads to sufficient improvement so that the solution converges, eventually.

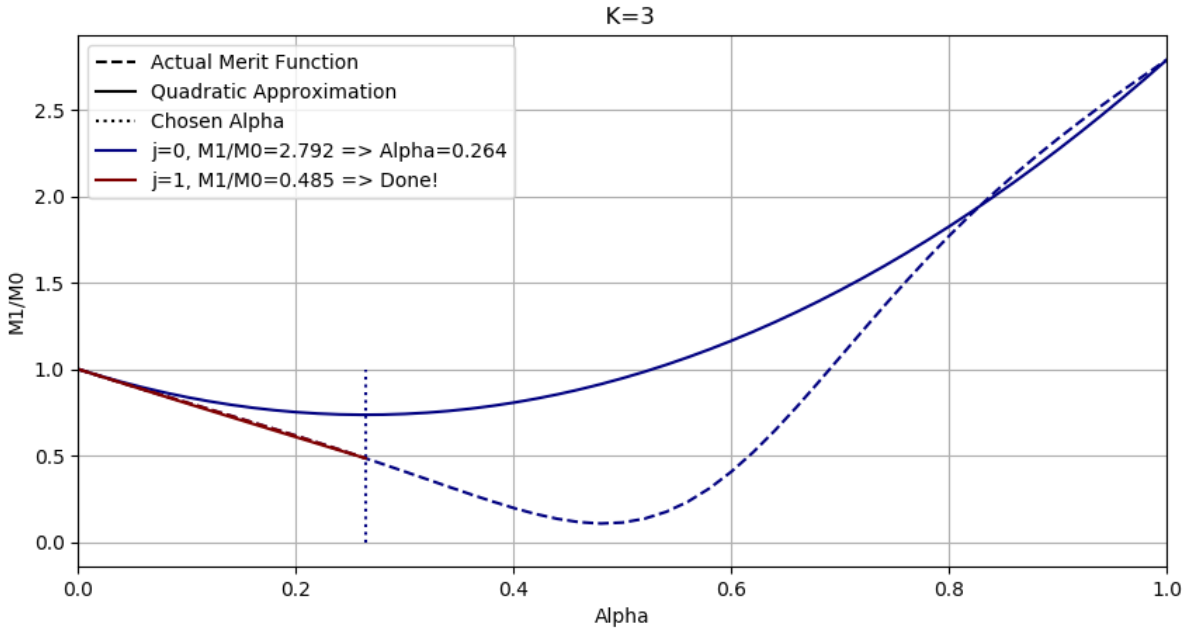

Figure 24- Quadratic approximation compared with the actual merit function curve. Hosford mode, n=8

With increasing the exponent a, the curvature of yield surface near to the principal stress axes increases. It has been observed in previous studies [7, 15] that the Newton-Raphson algorithm faces difficulty when processing stress states that return to such areas. The generated iteration maps presented in the previous chapter approve this observation. With higher exponents, the Newton algorithm's success becomes limited to only the stress states that will converge with the simple radial return, without much need for changing the plastic flow direction.

Figure 25 shows another example when the Hosford model with the exponent of 100 is applied. This case provides a better explanation for the divergence when a full Newton step is taken. The value of the merit function with full Newton step for this case is 7.3 times its value after the previous newton step, which emphasizes on the fact that how a significant change of the flow direction with a small change in the stress state can prevent the algorithm from finding the correct flow direction when using higher exponents.

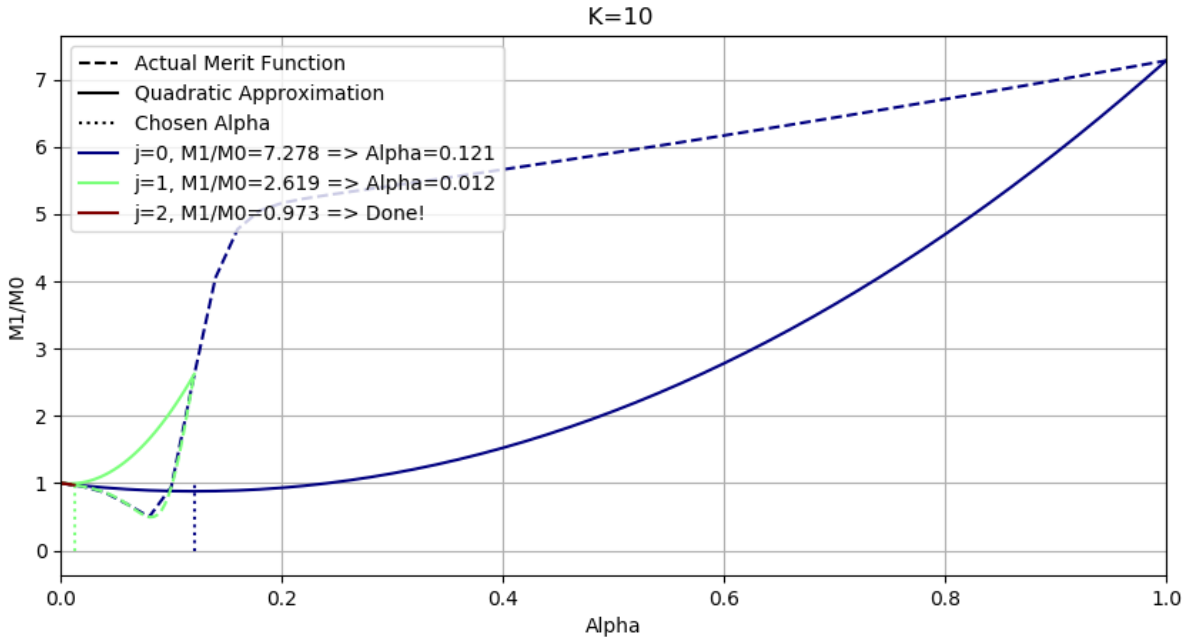

Figure 25- Quadratic approximation compared with the actual merit function curve. Hosford mode, n=100

5.2 Potential for improvement

It goes without saying that the efficiency of the line search subroutine implemented in the Newton-Raphson algorithm is expected to directly affect the convergence behavior of the models. In an effort to qualify the level of this dependency, and to demonstrate the best achievable result by a perfect line search algorithm, iteration map of the Hosford model with the exponent 100 is generated using such value of α that truly minimizes the residuals. This approach not only can be used to estimate the potential for improvement of the line search algorithm but also provides information about the distribution of the true value of α that minimizes the residuals. For this purpose, the optimization and root-finding package from the scipy open-source library is used. As a scalar function, the merit function was asked to be minimized using the single variable of α bounded in [0,1] range, with the tolerance of 10^{-5} for α, using the "minimize_scalar" module. This module uses the Brent method to find a local minimum in this interval. Brent's Method combines the golden section search with parabolic interpolation. Parabolic interpolation fits a parabola through a selected set of points, then uses this parabola to estimate the function's minimum [20]. Figure 26 shows the result when such an approach is applied.

Quadratic approximation, although proven to be very effective for the studied models, still can not capture the true minimum as shown in figures 24 and 25. Comparing with figure 9, It can be seen that a perfect line search algorithm can considerably improve the convergence behavior. The iteration distribution graph of such a case, presented in figure 27, shows that all the trial stress states in the tested set are converged with less than 9 iterations with the average of ~6, while the average iteration to convergence for the same model, with quadratic approximation, is 16.

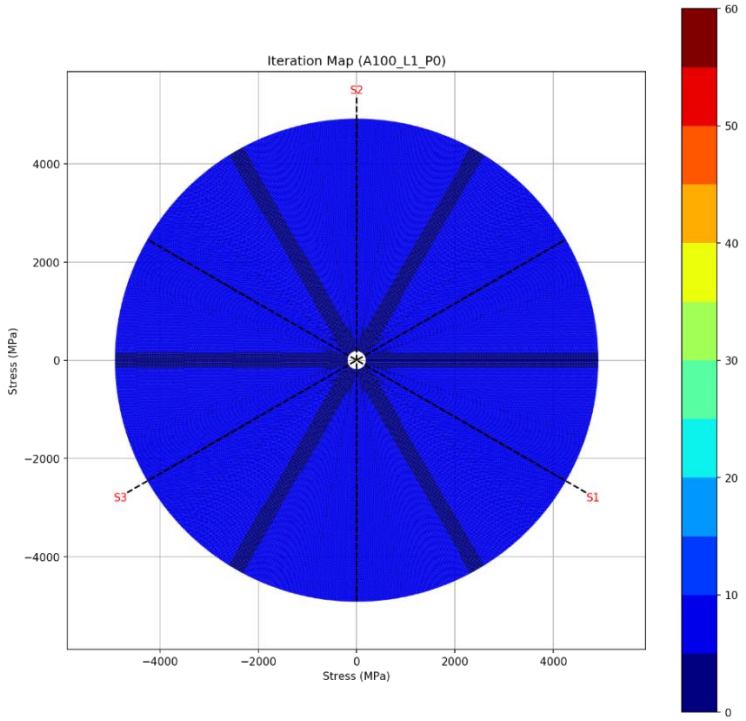

Figure 26- Iteration map for the perfect line search algorithm for Hosford model with the exponent of a=100

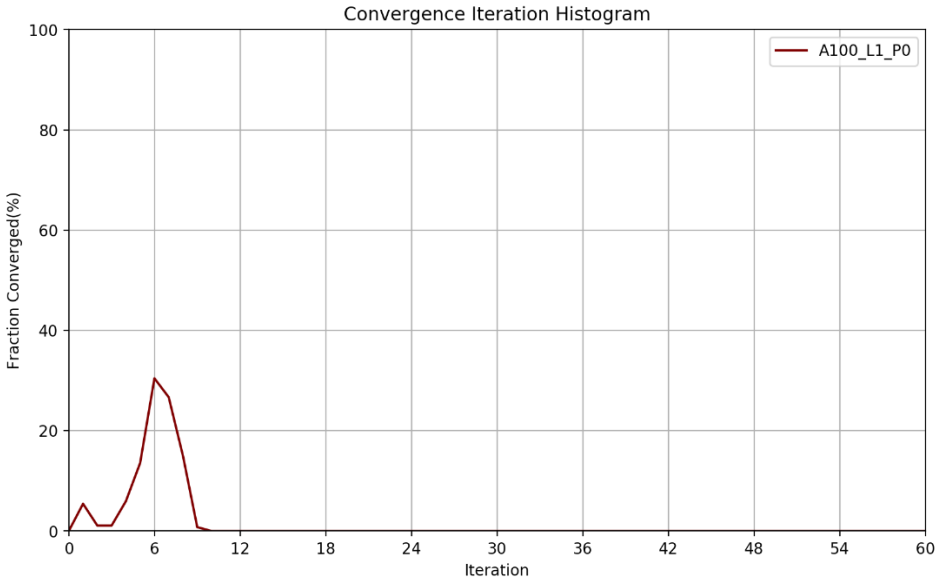

Figure 27- Iteration distribution for the perfect line search algorithm for Hosford model with the exponent of a=100

Applying the perfect line search approach using Brent's method, to the crystal plasticity model does approve the same conclusion. As can be seen in figure 28, the average number of iterations decreases drastically when the true minimum is found using Brent's minimizer algorithm. It appears that the exponent n does not affect the average iterations to convergence and all the points converge in almost 10 and 14 iterations with and without the projection modification, respectively.

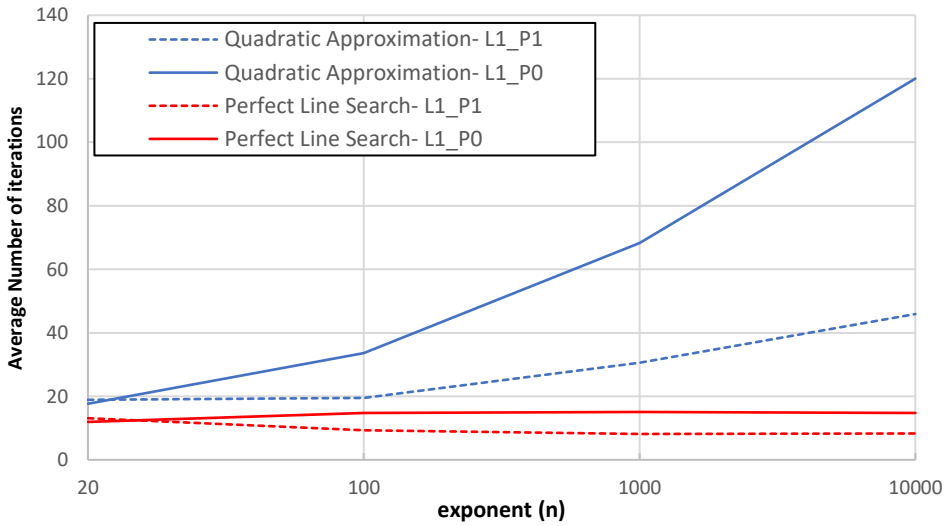

Figure 28- Average number of iterations for convergence for a point, with line search modification (quadratic approximation) for crystal plasticity model compared with the results of the perfect line search approach.

This is more emphasized comparing the iteration distribution graph of the two cases, one with quadratic approximation and the other applying the true minimizer module, as presented in figure 29. When using Brent's method, all the curves tend to show a peak at 10 to 15 with not much broadening, unlike the graphs generated from quadratic approximation results.

a) Line search with quadratic approximation

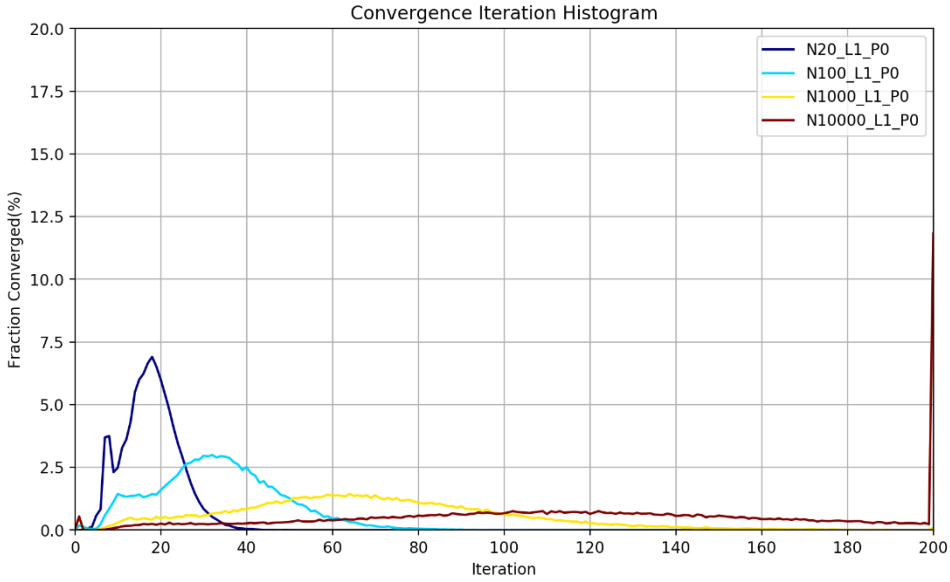

b) Perfect line search

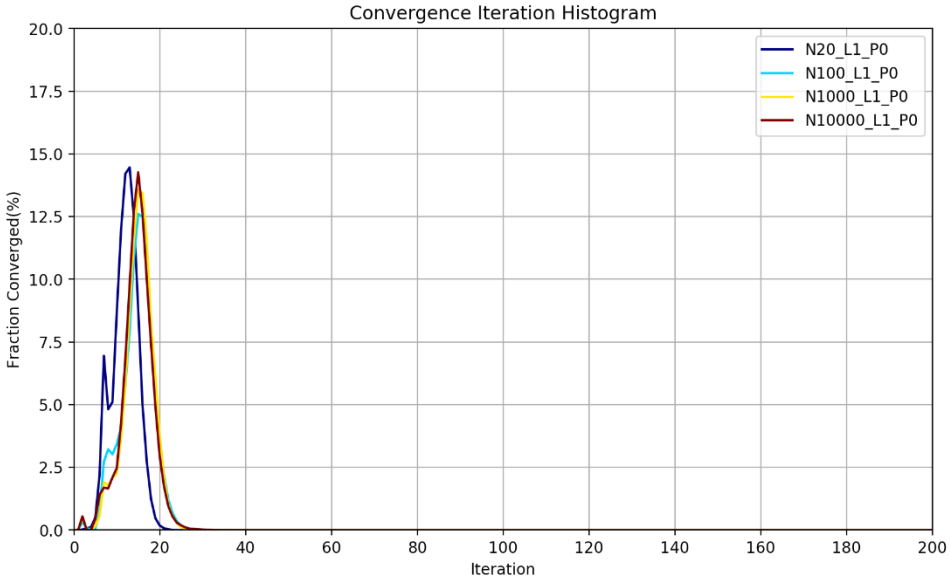

Figure 29- Distribution of the number of iterations for Crystal plasticity model, for different cases, compared to the same cases when applying the perfect line search approach

It is of interest to know how the distribution of the α value obtained by quadratic approximation differs from the value found by the Brent minimizer algorithm. Figure 30 shows this distribution plotted for both cases.

a) Line search with quadratic approximation

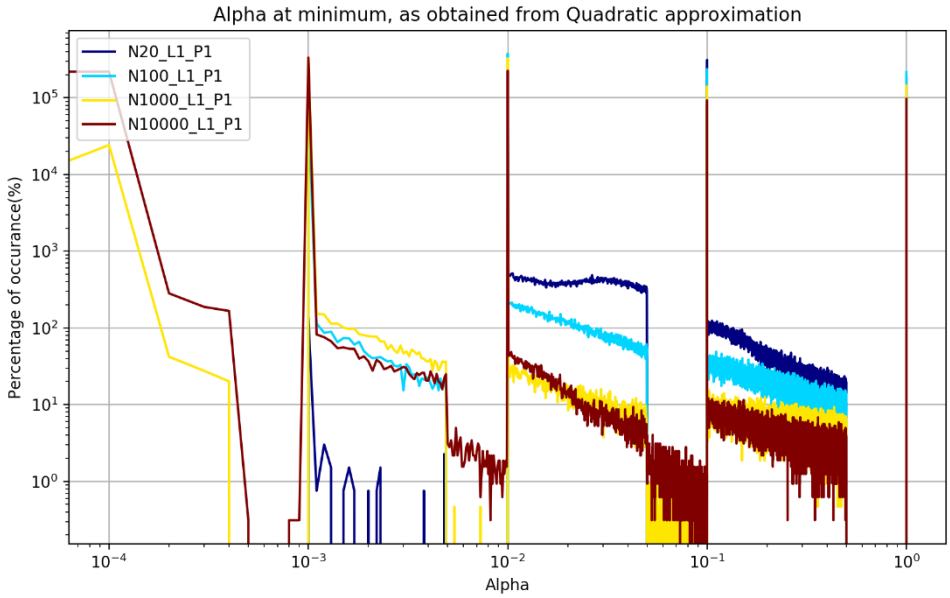

b) Perfect line search

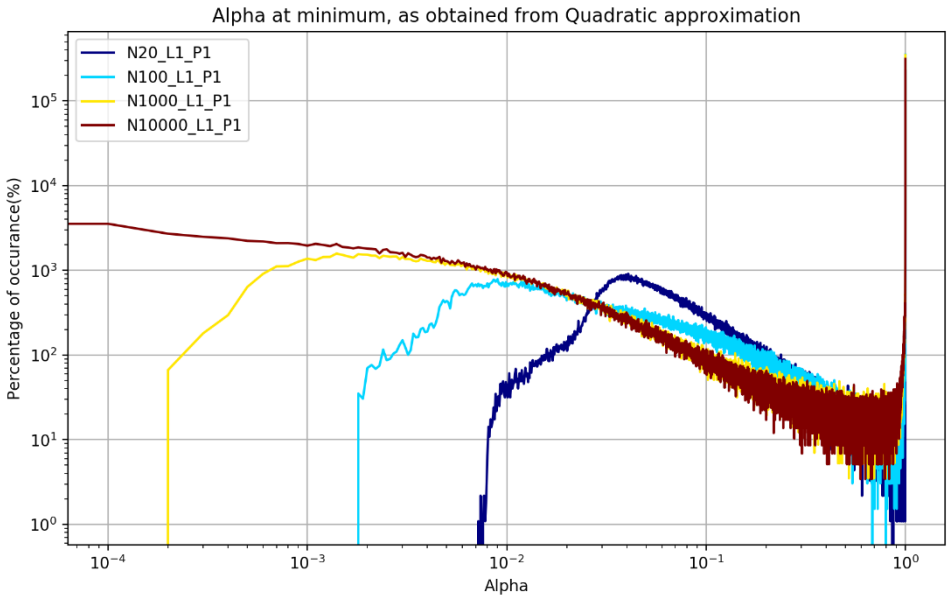

Figure 30- Distribution of the α value obtained by the line search algorithm, for Crystal plasticity model, for different cases, compared to the same cases when applying the perfect line search approach

As described in section 3.2, to avoid very small values of α, a condition is defined using a parameter denoted as η. The appearance of discrete peaks shown in figure 30-a is a direct result of this condition. The quadratic approximation can not capture the true minimum point when it happens to be in the range of 0.5 to 1. The perfect line search α distribution graph shows two distinct peaks for each curve. One α being 1 or very close to that which corresponds to the newton step and one on very small values of α in the range of 10^{-4} to 10^{-1}. This algorithm always finds a minimum for the merit function curve in the range of 0 to 1 which is expected considering its negative slope at α=0.

Figure 31 shows how detecting the true minimum can improve the convergence by visualizing the stress state after each Newton step on the π-plane. In the first step, quadratic approximation decides to continue with α=1 while the Brent algorithm detects the true minimum at α=0.72 and as a result, the subsequent steps require less correction.

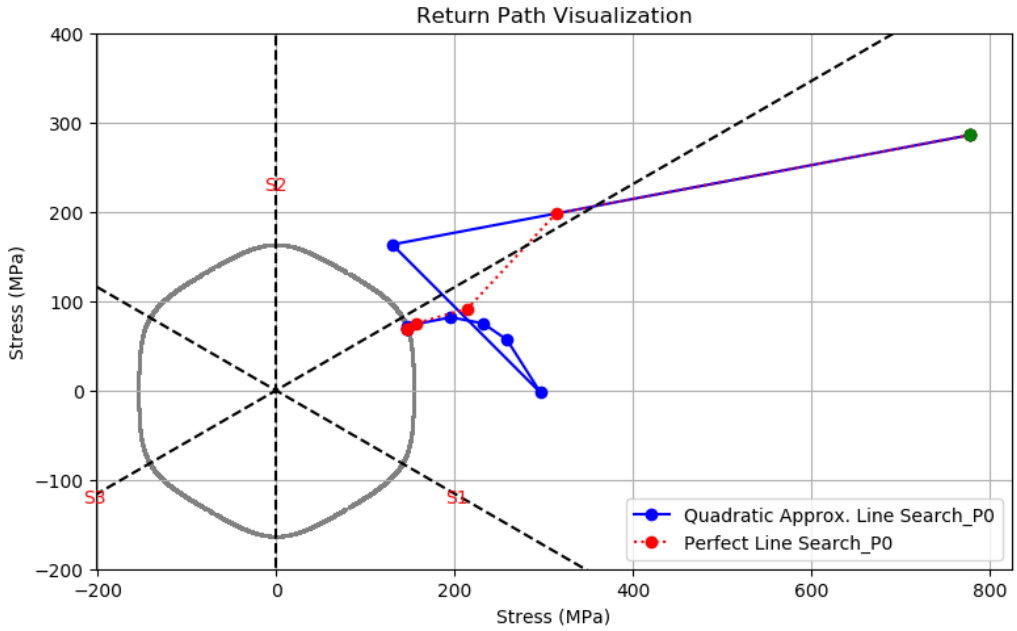

Figure 31- return path visualization for a test tensor. Hosford Model with the exponent of a=8 is applied to compare the perfect line search to the quadratic approximation.

It has been observed that Brent's algorithm requires almost 25 iterations for finding the α at the minimum point with the tolerance of 10^{-5}, which is much more than the quadratic approximation iterations (2-3 on average). But by reducing the newton iterations with a proper choice of α, it converges faster than the line search with the exponent n=10,000. A comparison between the analysis time for different cases is presented in figure 32. It should be mentioned

that this plot can vary if the algorithm is implemented using another programming language and the purpose is just to emphasize on the fact that detecting the true minimum point of the merit function, even with relatively higher computational cost in each step, can eventually reduce the number of iterations and therefore the computation time.

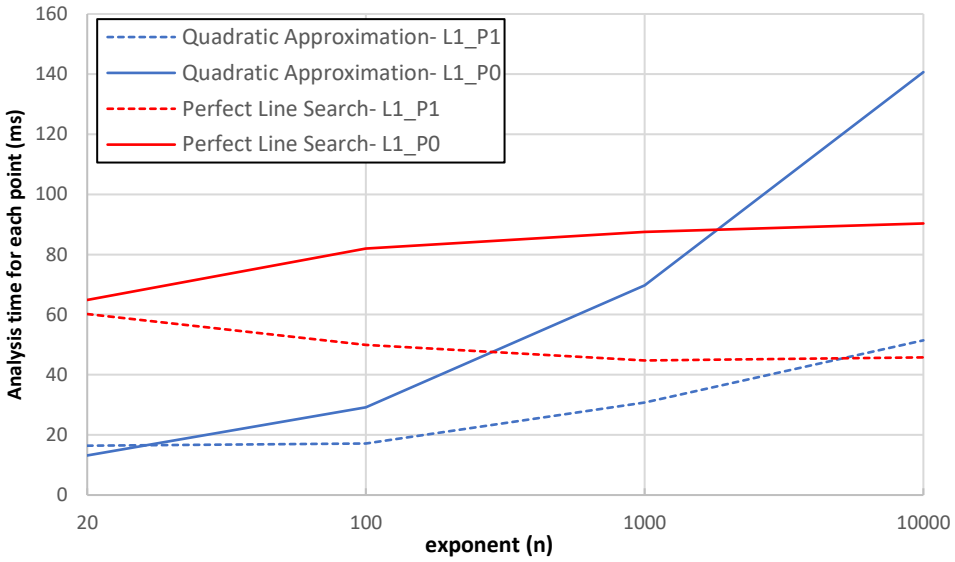

Figure 32- Comparison of the analysis time needed for each trial stress, when line search is employed against the Brent algorithm, referred to as the perfect line search here.

5.3 Projection of the trail stress

According to the results obtained for the Hosford model with a=8, using the projected trial stress as the initial guess has significantly improved the convergence behavior. Figure 33 shows the convergence path for the same discussed test tensor, compared with the case where the projected stress is used as the initial guess. When using the projected initial guess, the algorithm will have to mainly deal with decreasing the plastic residual since the yield function residual is already decreased with the projection, compared with the other case with trial stress far from the yield surface with a very high yield function residual.

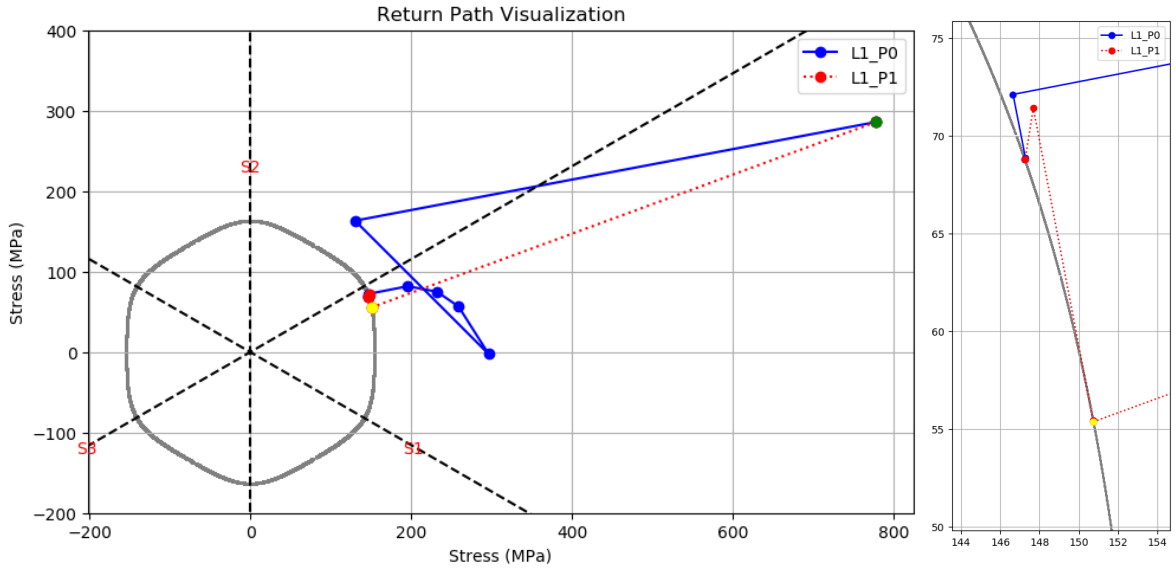

Figure 33- return path visualization for a test tensor for Hosford Model with the exponent of a=8, showing the effect of using the projected trial stress

6 Conclusions

The followings are the conclusions of the present study:

- Using the Mandel notation comes with a significant improvement in the running speed of the algorithm. For instance, carrying a double production operation between a fourth-order stiffness tensor and a second-order strain tensor is almost 30 times faster when using Mandel-converted second-order stiffness tensor and strain vector.
- A line search subroutine with a quadratic approximation is implemented for the Newton-Raphson algorithm to solve the return mapping problem for the isotropic Hosford model. the results of this implementation were compared against a study investigating the same model using the same parameters. The comparison validated the present implementation, providing the basis for applying it to the crystal plasticity model, which was the main goal of this study.
- For the Hosford model with the model parameter of a=6,8,100, applying the line search modification to a large set of points uniformly distributed in 5-dimensional stress space showed a significant improvement in convergence behavior The algorithm successfully handles all the trail stress states with up to f=60.
- For typical exponents in continuum plasticity, 6-12, improving the first guess by using the projected trail stress instead, significantly reduces the calculation time by decreasing the required Newton iterations.
- The return mapping algorithm with line search modification is also tested for the crystal plasticity model. The observations show a very limited capability for the Newton algorithm even for lower exponents. Line search modification has improved the convergence behavior significantly to the extent that up to n=300, full convergence for the analyzed set of points is achieved.
- The effect of improving the first guess on increasing the reliability as well as the efficiency of the algorithm is emphasized with applying on the crystal plasticity model, particularly for higher exponents. For n=10000, All the tested stress states are converged in less than 120 iterations with an average of 46 iterations per point when using the projected first

guess. For n=300, using projection modification has decreased the average iteration numbers from 46 to almost half.

- The efficiency of quadratic approximation is tested with comparing it against another subroutine which was capable of detecting the minimum point with high precision. The quantitive comparison suggests that the quadratic approximation, although proven to be very effective for the studied cases, is not the excellent method for improving the Newton solution. For all the exponents of 20 to 10,000, the alternative tested method resulted in fewer newton steps with the difference in required newton steps increasing with using higher exponents. For the case of n=10,000, this difference is large enough to make the overall solution faster when the alternative method is employed for finding the optimum vale of α.

7 References

1. Bower AF. Applied Mechanics of Solids. 2010.

2. Rees DWA. Basic Engineering Plasticity: An Introduction with Engineering and Manufacturing Applications. Oxford: Oxford: Elsevier Science & Technology; 2006.

3. Irgens F. Continuum Mechanics. 1. Aufl. ed. Berlin, Heidelberg: Berlin, Heidelberg: Springer-Verlag; 2008.

4. Elliotis M. A Finite Element Approach for the Elastic-Plastic Behavior of a Steel Pipe Used to Transport Natural Gas. Conference Papers in Energy. 2013;2013:1-10.

5. Hosford WF. A Generalized Isotropic Yield Criterion. Journal of Applied Mechanics. 1972;39(2):607-9.

6. LAPACK Users' Guide, Third Edition, http://www.netlib.org/lapack/lug/.

7. Scherzinger WM. A return mapping algorithm for isotropic and anisotropic plasticity models using a line search method. Computer Methods in Applied Mechanics and Engineering. 2017;317:526-53.

8. Prüger S, Kiefer B. A comparative study of integration algorithms for finite single crystal (visco-)plasticity. International journal of mechanical sciences. 2020;180:105740.

9. Dieter GE. Mechanical metallurgy. SI metric ed. ed. Bacon D, editor. London: McGraw-Hill; 1988.

10. Khan AS, Huang S. Continuum theory of plasticity. New York ; Chichester: Wiley; 1995.

11. Courtney TH. Mechanical behavior of materials. 2nd ed. ed. Boston: McGraw Hill; 2000.

12. Reed-Hill RE, Abbaschian R. Physical metallurgy principles. 3rd ed. ed. Boston: PWS-Kent; 1992.

13. Versino D, Bennett KC. Generalized radial-return mapping algorithm for anisotropic von Mises plasticity framed in material eigenspace: Generalized radial-return mapping algorithm. International journal for numerical methods in engineering. 2018;116(3):202-22.

14. Simo JC, Hughes TJ. Computational Inelasticity. Secaucus: Secaucus: Springer-Verlag; 1998.

15. Pérez-Foguet A, Armero F. On the formulation of closest-point projection algorithms in elastoplasticity-part II: Globally convergent schemes: ELASTOPLASITICITY-PART II:

GLOBALLY CONVERGENT SCHEMES. International journal for numerical methods in engineering. 2002;53(2):331-74.

16. Luenberger DG, Ye Y. Linear and nonlinear programming. New York: Springer; 2008.

17. Malvern LE. Introduction to the mechanics of a continuous medium. Englewood Cliffs, N.J: Prentice-Hall; 1969.

18. Zhang K. Multi-level Modelling of Plastic Anisotropy of Aluminium Alloys Using Crystal Plasticity Models and Advanced Yield Functions. Norges teknisk-naturvitenskapelige universitet, Fakultet for naturvitenskap og teknologi, Institutt for materialteknologi; 2014.

19. Logan RW, Hosford WF. Upper-bound anisotropic yield locus calculations assuming 〈111〉-pencil glide. International Journal of Mechanical Sciences. 1980;22(7):419-30.

20. Press WH. Numerical recipes in Fortran : the art of scientific computing. 2nd ed. ed. Cambridge: Cambridge University Press; 1992.

8 Appendix A - σ_{11}-σ_{22}-plane iteration map and yield surface for crystal plasticity model

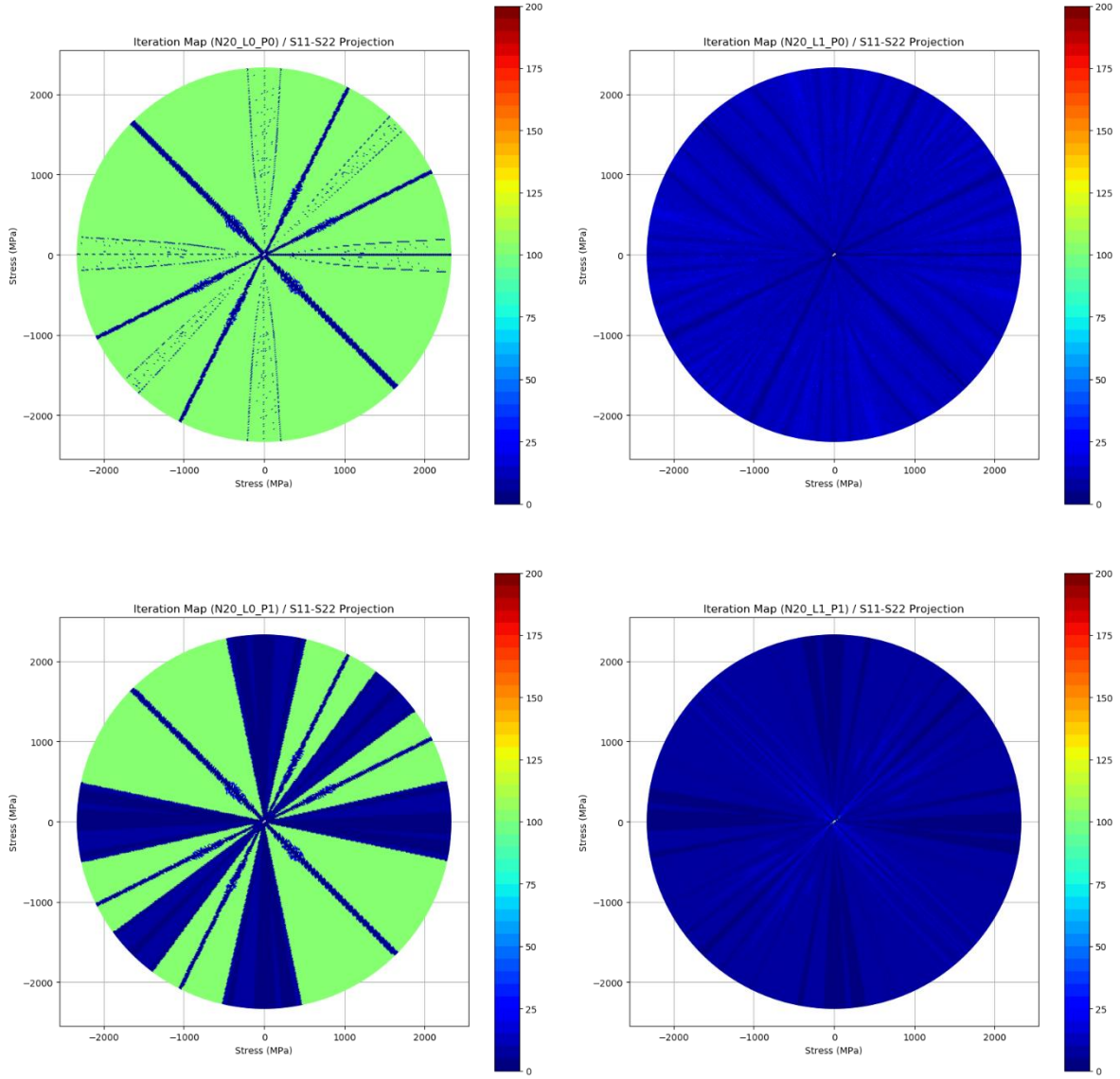

Figure 34- Iteration Map graphs for Crystal plasticity model, with exponent n=20

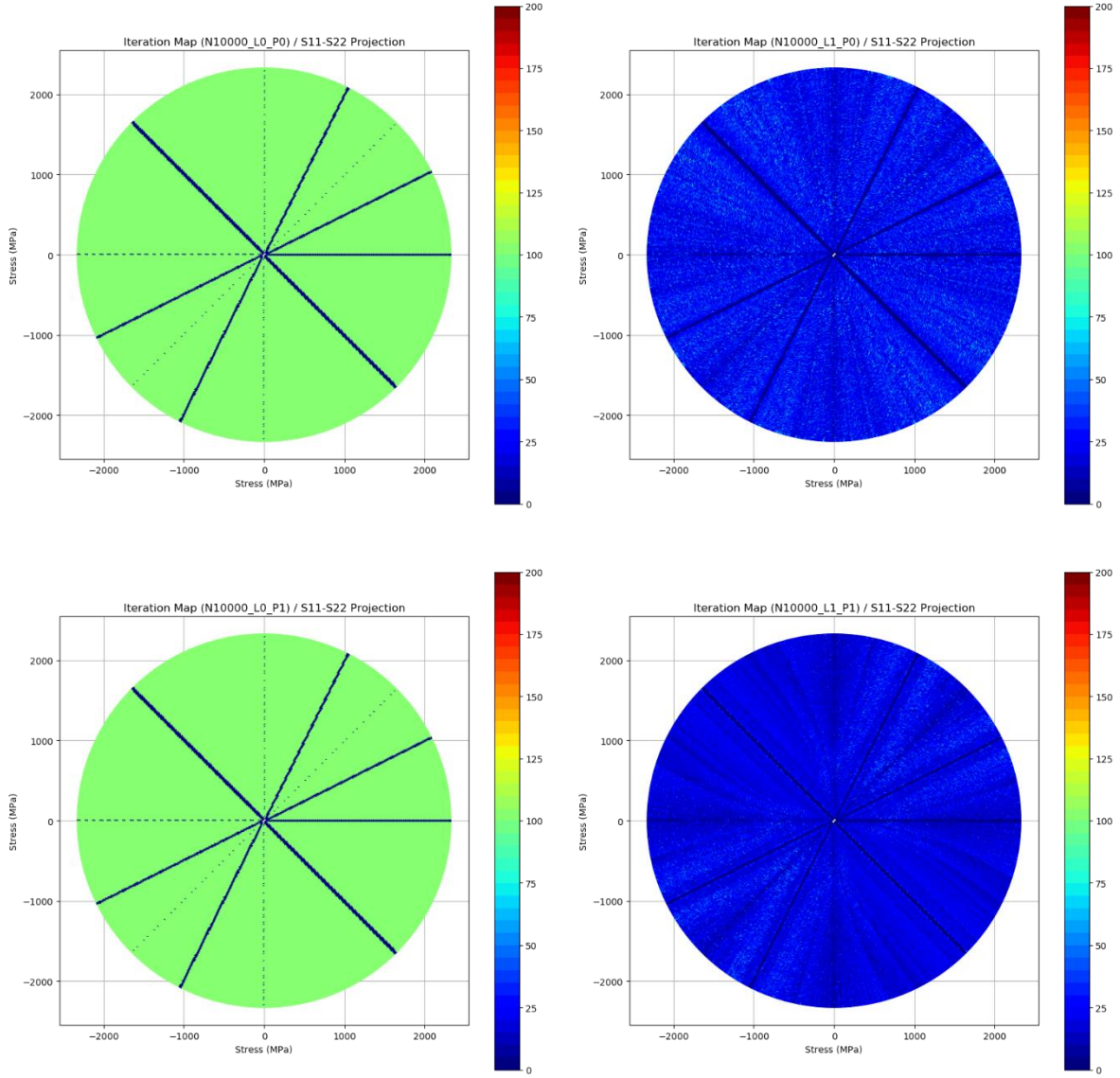

Figure 35- Iteration Map graphs for Crystal plasticity model, with exponent n=10,000

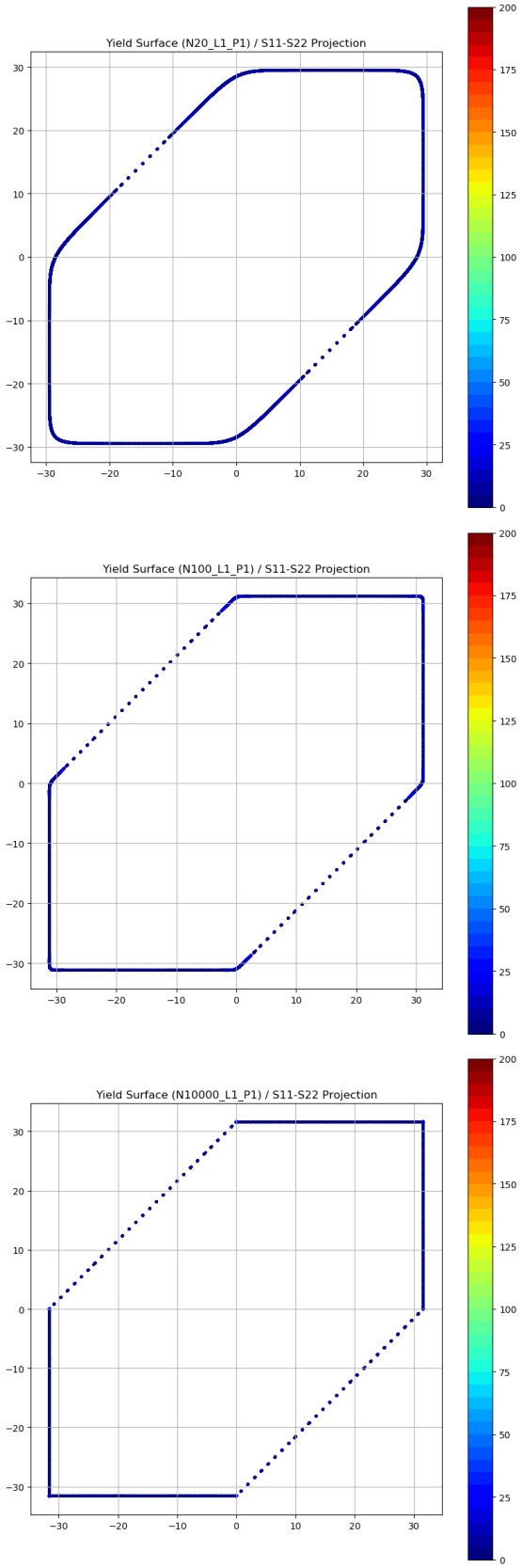

Figure 36- The generated yield surfaces by crystal plasticity model, with different exponents of 20,100,10000 for L1_P1 configuration